Journal of Membrane Science 657 (2022) 120663

Contents lists available at ScienceDirect

Journal of Membrane Science

journal homepage: www.elsevier.com/locate/memsci

Photocatalytic antifouling nanohybrid polysulfone membrane using the synergetic effect of graphene oxide and SiO_2 for effective treatment of natural rubber-laden wastewater

Tutuk Djoko Kusworo [a,*], Andri Cahyo Kumoro [a], Nita Aryanti [a], Dani Puji Utomo [a], Hasrinah Hasbullah [b], Fadhilah Fatma Lingga [a], Ade Widiastuti [a], Monica Yulfarida [a], Febio Dalanta [a], Tonni Agustiono Kurniawan [c]

[a] Department of Chemical Engineering, Faculty of Engineering, Diponegoro University, Semarang, 50275, Indonesia
[b] School of Chemical and Energy Engineering, Faculty of Engineering, Universiti Teknologi Malaysia, 81310, Skudai, Johor, Malaysia
[c] College of the Environment and Ecology, Xiamen University, Xiamen, 361102, Fujian, PR China

ARTICLE INFO

Keywords:
Photocatalytic membrane
Antifouling
COD removal
Ammonia removal
Wastewater treatment

ABSTRACT

This study investigates the effects of graphene oxide (GO) and SiO_2 composite as nano-photocatalysts in the polysulfone (PSf) membrane to treat natural rubber-laden wastewater (NRW) treatment under UV irradiation. The membranes were fabricated using the phase inversion process. Characterization results showed that the incorporation of GO and SiO_2 nanoparticles as a composite successfully changed the properties of the membranes. Optical analysis tests revealed that the composite enhanced the photocatalytic activity and possessed bandgap energy of 3.25 eV, which made the SiO_2 more active under UV light exposure after incorporating the GO. The addition of GO/SiO_2 to the membrane resulted in more hydrophilic properties with contact angle of 60.34° and water uptake ability of 52.78%. Conducting filtration under UV irradiation using PSf/GO/SiO_2 membrane exhibited a remarkable improvement in permeate flux by 129% from 9.85 L m^{-2} h^{-1} to 22.55 L m^{-2} h^{-1} and maintained 85.4% of permeate flux stability. With respect to removal performance, under the photo-filtration process, chemical oxygen demand (COD) removal increased from 73 to 84%, and ammonia-nitrogen (NH_3–N) removal improved from 78 to 92%. The photocatalytic kinetic evaluation suggested that the pseudo-first order kinetic model had a better fit than the zero-order kinetic. Regeneration tests showed that the PSf/GO/SiO_2 membrane has outstanding durability. The resistance during filtration and antifouling potential evaluations revealed that the GO/SiO_2 composite under UV light irradiation during filtration remarkably reduced the fouling formation and generated a high flux recovery ratio. This implies that this PSf/GO/SiO_2 membrane is promising for advanced treatment of NRW.

1. Introduction

On a global scale, Indonesia is one of the highest producers of natural rubber commodity. This rubber industry activity specifically in natural rubber mills, generates wastes in the forms of solid crumbs, rubber waste, and a large amount of wastewater called natural rubber-laden wastewater (NRW) [1]. The NRW possess serious threats to the environment due to its dangerous chemicals content. Typical characteristics of NRW contain 150–15,000 mg/L of chemical oxygen demand (COD), 300–5000 mg/L of total suspended solids (TSS), 300–3500 mg/L of total dissolved solids (TDS), high turbidity (>30 NTU), ammonia concentration of 100–1000 mg/L, and other organic matters such as lipids, cellulose, carotenoids, latex microparticles, and proteins with varying composition [2].

Over the past years, this wastewater is commonly treated using biological treatment [3] and coagulation-flocculation [4] prior to its disposal to the environment. Nonetheless, these methods generate sludge as a by-product that requires further treatment before being landfilled. This post-treatment contributes to an increasing operational cost for wastewater treatment. In recent years, membrane technology has been widely implemented for wastewater treatment due to its outstanding removal performances [5]. Its advantages include

* Corresponding author.
E-mail address: tdkusworo@che.undip.ac.id (T.D. Kusworo).

https://doi.org/10.1016/j.memsci.2022.120663
Received 14 March 2022; Received in revised form 10 May 2022; Accepted 17 May 2022
Available online 27 May 2022

continuous separation, efficient and clean energy consumption, versatility to be integrated with other physicochemical separation, and no sludge generation [5–7]. However, membrane technology is susceptible to fouling problems, which when a solution or particle is deposited on the membrane surface or pore that subsequently reduces the permeate flux and selectivity [8]. Membrane fouling can be induced physically (e.g., drag permeation, shear force) or chemically (e.g., hydrophobic interactions, ion binding effects) [8,9].

A variety of strategies have been applied to deal with membrane fouling by using nanofiltration membranes based on polyelectrolyte multilayers [10]. A preliminary study reported that incorporating selective materials into polymeric membranes was effective and practical to improve membrane anti-fouling ability [10]. Hydrophilic polymers such as polyvinyl alcohol (PVA), polyethylene glycol (PEG), and others can be coated onto the membrane to reduce the formation of fouling [11–14]. Additionally, inorganic nanoparticle incorporation can also be implemented to reduce the fouling tendency of the such as titanium oxide (TiO_2) [15], zinc oxide (ZnO) [16], graphene oxide (GO) [17], iron oxide (Fe_3O_4) [18], zirconium oxide (ZrO_2) [19], aluminum oxide (Al_2O_3) [20], and silicon dioxide (SiO_2) (Wu et al., 2014a).

In this work, graphene oxide (GO) was utilized as a membrane filler due to its superior thin sheet strength, easy dispersion in water or organic solvents, and being compatible with a ceramic or polymer matrix [22]. GO could give a higher hydrophilicity to the membranes based on a high-water volumetric flux [23]. However, the GO alone hardly achieve the capability of overcoming fouling on the membrane surface. To overcome the bottlenecks, the GO needs to be integrated with other materials to promote the formation of the carboxyl group on the membrane surface so that they do not adhere to undesirable foulants during treatment. GO nanomaterials have been reported to form a nanohybrid membrane composite with Fe_3O_4, TiO_2, and ZnO and obtained excellent membrane performance antifouling property [18,24,25]. It has been reported that the flux recovery ratio (FRR) of the PSf mixed matrix Fe_3O_4/GO nanohybrid membrane reached 95% due to the synergistic effects of Fe_3O_4 and GO in the polymeric membrane that enhanced water flux, membrane retention, and antifouling properties [18]. Although the addition of inorganic materials into polymeric membranes could induce micro-void formation between the polymeric chains and the surface of inorganic material, resulting in higher selectivity [26], this nanocomposite still needs to undergo aggregations, which could reduce membrane performance [11,27]. In addition, the nanoparticle incorporation to the membrane is still not enough to improve and prolong the hydrophilicity and antifouling properties of the membrane.

To improve the antifouling performance of the nanohybrid membrane, the authors created a seminal photocatalytic membrane by coating the membrane's surface with other materials [28]. Some chemicals have semiconductor material characteristic such as TiO_2, ZnO, WO_3, Fe_3O_4, C_3N_4, SiO_2, CeO_2, Bi_2WO_6 and GO [28–38]. Among them SiO_2 based materials have appeared as one of the popular nanofiller for polymeric membranes due to their outstanding chemical, thermal, and mechanical stabilities as well as the highly hydrophilic properties. Some literatures reported that the hydrophilic property of SiO_2 attributed the membranes with higher permeability, hydrophilicity, and antifouling properties [39,40]. Unfortunately, in optical properties SiO_2 has a drawback that it cannot perform a good photo-degradation due to its large bandgap energy (>5.0 eV) [41,42]. As a result, SiO_2 alone might not achieve the photocatalytic ability. Some methods have been carried out including such as heterojunction patterns, metal decorations, metal-organic frameworks, and non-metal materials addition to improve the semiconductor properties [29,30,41–43]. It is reported that the GO addition into GO/TiO_2 membrane composite that has a large surface area, sensitive increment, photocatalytic properties, and fast charge transport [24,44]. The combination of ZnO with GO in a nanohybrid PVC/GO-ZnO membrane has successfully reduced the tendency of fouling and can perfectly maintain a stable permeate flux at 120 L m^{-2} h^{-1} [25]. The fancy electronic characteristics of GO can facilitate the electron motions and can decrease the electron/hole recombination, which resulted in an enhanced photocatalytic activity. It is expected that the synergetic effects of GO and SiO_2 can attribute the fabricated membrane with not only higher hydrophilicity but also better photocatalytic activity to enhance membrane performance as well as improving the antifouling ability.

To the best of our knowledge, none has studied the synthesis, characterization, and performance evaluation of photocatalytic polysulfone (PSf) membrane-embedded by GO and SiO_2 nanoparticles as the photocatalysts for an integrated photocatalytic and membrane filtration process of NRW treatment under UV light exposure. The membrane characteristics were comprehensively characterized. This study also evaluated and compared the membrane performance in the dark conditions and under UV light exposure, The photocatalytic degradation kinetics, regeneration test, fouling resistances, and antifouling properties of the membranes were also studied. It is expected that this study would provide a better option of membrane filtration to tackle fouling problem and extend the membrane's lifetime for an effective NRW treatment.

2. Materials and methods

2.1. Materials

Polysulfone (PSf, 99%) pellets (UDEL ® PSU P-1700 NT) as the primary membrane material was obtained from Solvay Advanced Materials, USA. N-methyl-2-pyrrolidone (NMP, 99.9%) as the solvent to dissolve the PSf pellet was supplied by Merck, Germany. Silicon dioxide nanoparticles (SiO_2, 99%) were provided by Nano Center Indonesia. Graphite powders (99.5%) as the raw material for graphene oxide (GO) synthesis was obtained from Shanghai Chemicals, China. Sulfuric acid (H_2SO_4, 98%) and potassium permanganate ($KMnO_4$, 99%) as required chemicals in GO synthesis were supplied by Merck, Germany. The sample of natural rubber-laden wastewater (NRW) was collected from PTPN VII located in Bengkulu, Indonesia. The detailed characteristics of the wastewater are presented in Table S1. Deionized (DI) water was used in chemical solution preparation and all experiment.

2.2. Preparation of nanocomposite membranes

The PSf/GO/SiO_2 membrane films were prepared based on non-induced phase inversion. Graphene oxide (GO) used in this study was synthesized by the modified Hummer's method, conducted in our previous work [44]. The variation of nanoparticles in membrane preparation are listed in Table S2. The nanoparticles of GO and SiO_2 were dispersed in NMP solvent in a separate chamber using an ultrasonic homogenizer at a frequency of 40,000 Hz for 60 min. After both solutions were ready, the PSf and the nanoparticle dispersion were poured and stirred for 12 h at an ambient temperature. The generated mixture was transferred into an ultrasonic bath at 60,000 Hz at 50 °C for 60 min to remove the trapped bubbles inside the solution. Then, the nanohybrid membrane solution was cast onto a glass plate using a casting knife. The casted membrane film was then immersed in a DI water bath to remove the solvent and generate the membrane film. The generated membrane films were immersed in another DI water bath for 24 h and then were dried at an ambient temperature.

2.3. Characterization

Scanning electron microscopy (SEM, JEOL Series, JSM-6510-LA, Japan) was performed to observe the micromorphology of GO and SiO_2 nanoparticles. The particle size distribution of GO and SiO_2 were determined using particle size analyzer (PSA, SALD®201, Shimadzu, Japan). It was also used to capture the surface and cross-sectional images of the fabricated membranes. Energy dispersive x-ray (EDX, JEOL

Series, Japan) was used to observe the chemical composition of the fabricated membrane and also the mapping distribution of some elementals. The chemical functional groups of the nanoparticles and the fabricated membranes were analyzed using Fourier-transform Infrared (FTIR, PerkinElmer, USA). X-ray Diffraction analysis (XRD, Shimadzu, Japan) was used to examine the crystallinity of the composite and their impact on the crystalline characteristics of the fabricated membranes. The optical analysis of diffuse reflectance spectrometry (DRS) was carried out by using a UV–vis (ultraviolet–visible) spectrophotometer (UV–vis Spectrophotometer, Shimadzu, Japan). The energy gaps of the nanoparticle were then estimated using the method of Tauc plot. The surface charge of the nanoparticles was observed based on point of zero charge (PZC). The porosity measurement of the membrane was carried out by immersing the membrane for 24 h in distilled water and recording the final weight of the membrane that finally calculated using Eq. (1) [2].

$$\varepsilon = \frac{w_f - w_i}{\rho_w \times A \times \delta} \times 100\% \quad (1)$$

where: ε is the membrane porosity (%), while w_f and w_i represent the weights of the wet and dry membranes, respectively (g). ρ_w shows the water density at room temperature (0.997 g cm^{-3}); A corresponds to the effective surface area (cm^{-2}); δ represents the membrane thickness (cm).

Additionally, the average pore radius was analyzed using the Guerout-Elford-Ferry approximation by Eq. (2) [2].

$$r = \sqrt{\frac{8\eta\delta Q \times (2.9 - 1.75\varepsilon)}{\varepsilon \times A \times \Delta P}} \quad (2)$$

where: η shows the water viscosity at room temperature (8.9×10^{-4} Pa s), δ represents the membrane thickness (m), Q is the volumetric flow rate of the permeate (m^3. s^{-1}), and ΔP shows the *trans*-membrane pressure (Pa).

The material testing machine (UTS H001, China) was used to carry out the membrane mechanical strength measurements based on thickness tensile strength, and elongation break. As a critical factor of membrane performance, surface hydrophilicity was determined through water contact angle. A contact angle meter (RASE angle meter, Japan) was utilized to measure a static contact angle by employing the sessile drop method. The method for calculating water uptake and membrane's affinity was followed from Ref. [22]. The water uptake value of fabricated membranes was calculated using Eq. (3).

$$W_U = \frac{w_w - w_d}{w_d} \times 100\% \quad (3)$$

where: W_U is the water uptake (%), w_w and w_d are the wet and dry weights of the tested membrane (g).

Further, the membrane's affinity towards liquid was measured using a theoretical Flory-Huggins model, represented in Eqs. (4) and (5).

$$\varphi = \frac{\left(w_w - w_d/\rho_s\right)}{\left(w_w - w_d/\rho_s\right) - \left(w_d/\rho_m\right)} \quad (4)$$

$$\chi = -\frac{\ln\varphi + (1-\varphi)}{(1-\varphi)^2} \quad (5)$$

where φ represents the volume fraction and χ represents the Flory-Huggins (FH) interaction parameter. ρ_s and ρ_m show the solvent (water) and membrane densities (g/cm^3), while w_w and w_d are the wet and dry weights of the tested membrane (g).

2.4. Photocatalytic performance of the fabricated membranes

The photocatalytic-filtration (photo-filtration) performance of the fabricated membranes was evaluated based on the permeate flux and pollutants removal in NRW photo-filtration process. The photo-filtration test was conducted using a prototype of a membrane filtration system equipped with a feed tank, a pump, pressure gauge, a permeate collector, and a membrane cell modified with a UV lamp (Philips TUV- 30-W, Netherland). Fig. 1 shows the photo-filtration cross-flow module setup used in this particular experiment. The UV lamp can be easily turned on or off to perform, whether on dark or UV exposure filtration. The actual sample of NRW was used as the feed for evaluating the permeate flux and pollutants rejection, which focused on COD and NH_3–N removals.

Prior to measuring the wastewater flux analysis, the membrane was acclimated using deionized water for 30 min. This test was performed at 5 bar *trans*-membrane pressure with a membrane area of 12.57 cm^2. The permeate flux was recorded every 30 min for 5 h for each membrane. The membrane water flux values were then calculated using Eq. (6).

$$J = \frac{V}{A.t} \quad (6)$$

where: J and V are the permeate water flux ($L.m^{-2}$. h^{-1}) and the volume of the permeate (L), at the same time, A and t are effective membrane area (m^2) and filtration time (h), respectively.

The COD concentration was determined based on the dichromate method, and the NH_3–N concentration was colorimetrically analyzed according to the Nessler's reagents. The following Eq. (7) was used to calculate membrane pollutant rejection.

$$R = \left(1 - \frac{C_P}{C_F}\right) \times 100\% \quad (7)$$

where: R is rejection efficiency (%), C_p and C_f are the concentration of the pollutant in permeate and feed solution, respectively (mg/L).

2.5. Photocatalytic activity of the PSf/GO/SiO_2 nanohybrid membrane

The photocatalytic activity of the fabricated membranes was evaluated by assessing the COD and NH_3–N degradation rate. Firstly, 100 mL of NRW sample was diluted by adding 100 mL of DI water to reduce the pollutant concentration. The membrane sheet with 5 cm in diameter was mounted onto the glass holder and immersed into 100 mL of NRW sample. This experiment was carried out in a dark and closed chamber equipped with a UV lamp. The complete illustration of the batch photocatalytic test setup is presented in Fig. S1. Before the UV lamp was turned on, the membrane was immersed for 60 min to achieve the adsorption equilibrium state. This photocatalytic process was conducted for 120 min, and the COD and NH_3–N removals were measured periodically every 20 min.

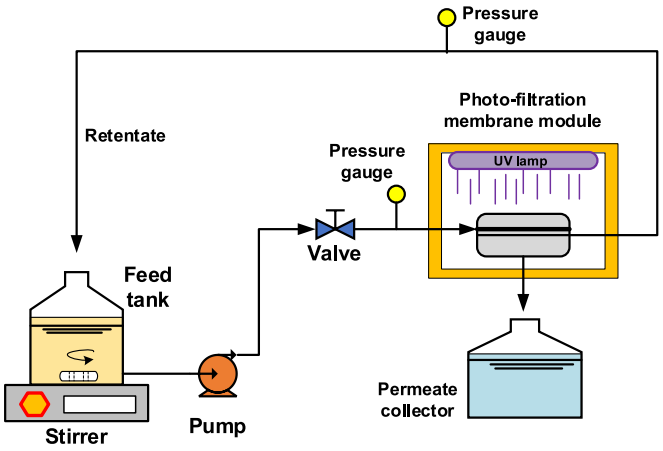

Fig. 1. Schematic illustration of membrane's photo-filtration experimental setup.

The photocatalytic degradation kinetics using PSf/GO/SiO_2 nano-hybrid membrane were further evaluated by applying the zero order and pseudo-first order kinetic models. The mathematical expressions of the applied kinetic models are represented in Eq. (8) and Eq. (9), respectively.

$$C_o - C_t = k_o t \tag{8}$$

$$\ln\left(\frac{C_o}{C_t}\right) = k_1 t \tag{9}$$

where: C_o and C_t represent the concentrations of pollutants at initial (mg/L) and at a specific time (mg/L), k_o (mg L^{-1} min^{-1}) and k_1 (min^{-1}) symbolize the rate constants of zero-order and pseudo-first order kinetic models, and t is the operating time (min).

2.6. Resistance during filtration and antifouling potential analysis

The resistance during filtration was measured by using resistance in series model. The model that takes into account every type of membrane fouling resistance, such as intrinsic resistance (R_m), adsorption resistance (R_a), deposition resistance (R_d), and concentration polarization (R_{cp}). The mathematical expressions of those resistances are shown in Eqs. 10–13, respectively [22].

$$R_m = \frac{\Delta P}{\eta \times J_i} \tag{10}$$

$$R_a = \frac{\Delta P}{\eta \times J_a} - R_m \tag{11}$$

$$R_d = \frac{\Delta P}{\eta \times J_f} - R_m - R_a \tag{12}$$

$$R_{cp} = \frac{\Delta P}{\eta \times J_v} - R_m - R_a - R_d \tag{13}$$

where: ΔP is the *trans*-membrane pressure (Pa), η is pure water viscosity (Pa.s), J_i, J_a, J_f, and J_v are the initial membrane pure water flux (PWF), the measured PWF after fouled by static adsorption, the PWF after fouled by actual NRW, and the measured flux when operating in actual NRW filtration, respectively.

The antifouling potential of the fabricated membranes was also assessed to measure the total fouling ratio (R_T), reversible fouling ratio (R_R), irreversible fouling ratio (R_{Ir}), and the flux recovery ratio (FRR), as Eqs. 14–17, respectively [22].

$$R_T = \left(\frac{J_{pw0} - J_{ww}}{J_{pw0}}\right) \times 100\% \tag{14}$$

$$R_R = \left(\frac{J_{pw1} - J_{ww}}{J_{pw0}}\right) \times 100\% \tag{15}$$

$$R_{Ir} = \left(\frac{J_{pw0} - J_{pw1}}{J_{pw0}}\right) \times 100\% \tag{16}$$

$$FRR = \left(\frac{J_{pw1}}{J_{pw0}}\right) \times 100\% \tag{17}$$

where J_{pw0} is the initial PWF. J_{pw1} is the PWF after cleaning. J_{ww} is the permeate flux of wastewater.

3. Results and discussion

3.1. Characterizations of fabricated membranes

3.1.1. Micromorphology of nanoparticles and fabricated membranes

The micromorphology of the applied nanoparticles, i.e., GO and SiO_2, was examined using scanning electron microscopy (SEM). It can be seen in Fig. S2(a) the SEM image of GO that the GO particles appeared close to rectangular shapes and consisted of the layered structure. These thin layers of GO can increase the effective surface area; therefore, increasing the availability of the active sites. The rich carbonyl and carboxyl groups on the surface of GO are also attributed to the increase of the hydrophilicity of this material. Fig. S2(b) shows the particle distribution of GO. It can be seen that GO has wide particle size distribution, which particle size of 300–350 nm is the dominant distribution with average size of 273.68 nm. Apart from this, Fig. S2(c) shows the SEM image of SiO_2 nanoparticles. This picture describes the micromorphology of the pristine SiO_2 that is applied as the nanofiller in the membrane. Based on the SEM image, it can be observed that SiO_2 nanoparticles distribute uniformly in considerably similar particle sizes, which has a dominant distribution at 60–80 nm with average size of 71.92 nm. However, at some points, the aggregation of SiO_2 particles still occurred. It is explainable by the high tendency of the nano-sized particles to stick with others and form aggregations. Consequently, in membrane synthesis, a well-known mixing technique and ultrasonication were essential for ensuring the aggregation did not form in the fabricated membranes.

To assess the effects of GO/SiO_2 addition in the membrane, SEM analysis was also carried out to capture the surface and cross-section micromorphology images of the fabricated membranes. The micromorphology of the membrane should be assessed due to its essential information regarding the physical characteristics and shapes of the membrane. This information has a strong relation to performance features of the membrane, such as selectivity and permeation properties. Fig. 2 depicts the SEM results of the fabricated membranes, including their surface and cross-sectional images. The surface image of a neat PSf membrane (Fig. 2(a)) shows a visually noticeable porous surface with several defects occurring on its surface. These defects might be generated during the phase inversion process due to the different rates of coagulation which can be slower than in other spots. These defects can promote unselective separation and reduce the pollutants rejection performance of the membrane. In the surface image with the wider magnification, the defects can be easily observed. Meanwhile, another SEM image of the neat PSf membrane in Fig. 2(c) reflects the micromorphology of the cross-section structure. It can be seen that the transverse structure of the neat PSf membrane dominantly consists of uncomplete finger-like structure at the top and a porous void structure at the bottom. These structures are the critical morphology for indicating an asymmetric membrane. The huge voids were captured in the cross-section of the neat PSf membrane, which led to the unselective voids that can possibly reduce the membrane selectivity [45].

Fig. 2(b) shows the surface image of the PSf/GO/SiO_2 membrane. It can be observed that the membrane surface is relatively darker than that of the neat PSf membrane. This might be due to the effect of GO loading to the membrane that resulted in darker surface color, as in agreement with another reported study. Some dots can also be seen on the membrane surface that strongly suggest the existence of GO/SiO_2 nanoparticles. It is defect-free on the membrane surface, and no aggregation structure is found. It indicates that the applied mixing technique and ultrasonication were successful in generating a perfectly dispersed dope solution. The existence of GO/SiO_2 nanoparticles on the membrane surface is desirable to perform the photocatalytic process when they are exposed to UV light. It is also desirable to increase the hydrophilicity to enhance the permeability of the membrane [27]. Additionally, Fig. 2(d) shows the cross-section picture of the PSf/GO/SiO_2 membrane. The cross-section structure is quite similar to the neat PSf membrane, which is an asymmetric membrane. Fortunately, the cross-section structure exhibited in PSf/GO/SiO_2 membrane was more well-arranged compared to the neat PSf membrane. This phenomenon was due to the effects of GO and SiO_2 nanoparticles loading on the membrane solution that further formed more gaps between the polymer chain, resulting in more creation of voids structure in the membrane's body. The embedded

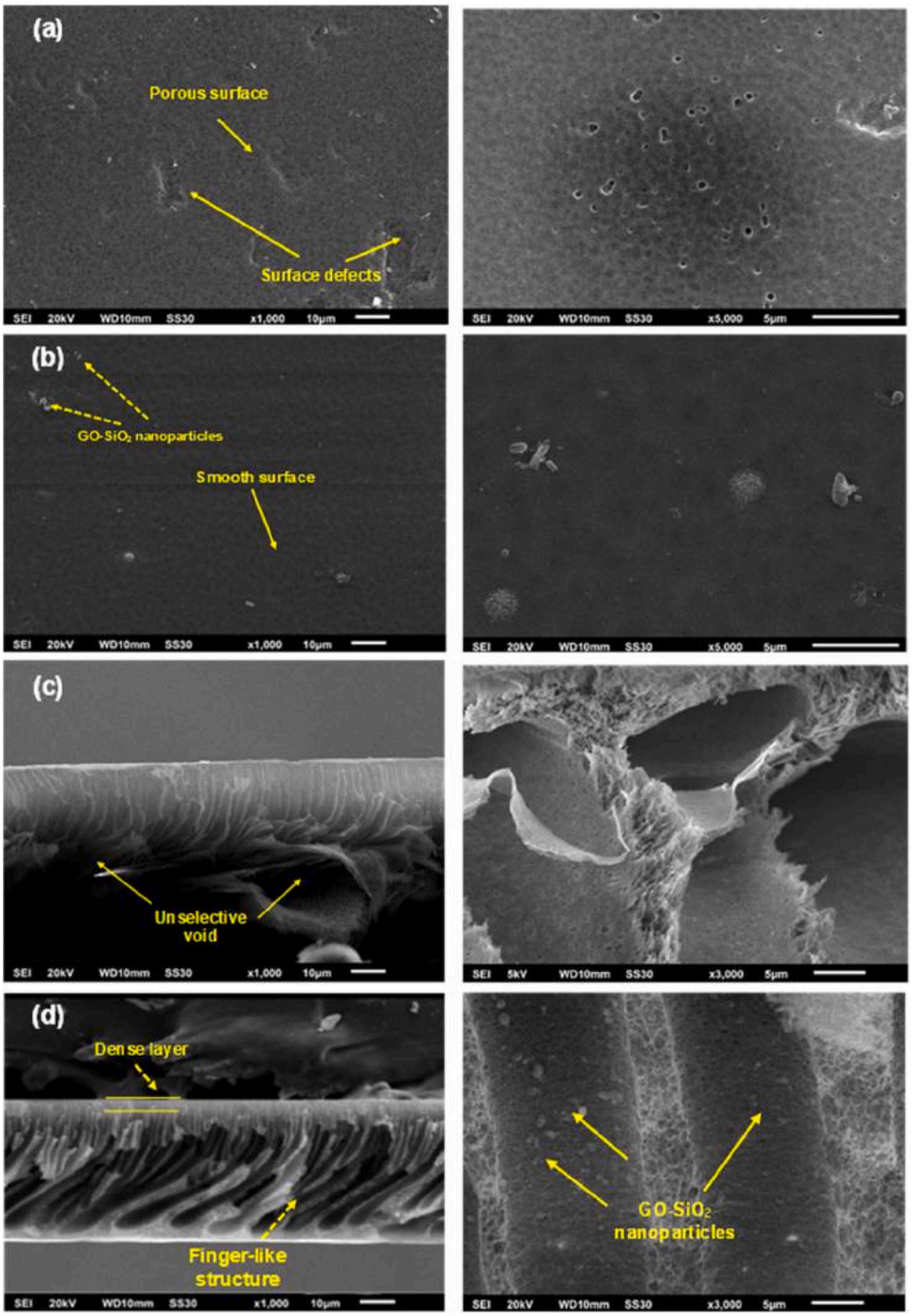

Fig. 2. SEM images with different magnifications of the (a) Surface of neat PSf, (b) Surface of PSf/GO/SiO_2 membrane, (c) Cross-section of neat PSf, and (d) Cross-section of PSf/GO/SiO_2 membrane.

Table 1
Chemical composition of the neat PSf and PSf/GO-SiO_2 membranes revealed by EDX analysis.

Elemental composition	Neat PSf		PSf/GO-SiO_2		Oxide composition of PSf/GO-SiO_2	Weight (%)	Mole (%)
	Weight (%)	Atomic (%)	Weight (%)	Atomic (%)			
Carbon (C)	83.45	88.95	78.26	84.63	C (elemental)	85.83	97.58
Oxygen (O)	11.09	8.87	16.03	13.26			
Sulfur (S)	5.46	2.18	4.99	2.02	SO_3	13.59	2.31
Silicon (Si)	–	–	0.41	0.06	SiO_2	0.56	0.10
Copper (Cu)	–	–	0.31	0.03	CuO	0.02	0.01

nanoparticles are also found in the cross-sectional structure of the membrane. It can be seen that the void structure in the PSf/GO/SiO_2 membrane is in the form of a finger-like structure. The finger-like structure is well-formed from the denser top layer to the bottom, with no unselective voids formed. This well-structured membrane can perform better selectivity and permeability.

EDX analysis was performed to reveal the chemical composition of the neat PSf and PSf/GO-SiO_2 membranes, as the results are listed in Table 1. Based on Table 1, it can be seen that neat PSf contains elementals of carbon (C), oxygen (O), and sulfur (S) with compositions of 83.45, 11.09, and 5.46%, respectively. Contrary, after the membrane's modification with GO-SiO_2, the membrane's composition significantly changed. It is recorded that the composition of silicon (Si) is detected at 0.41%, and the composition of oxygen increases from 11.09 to 16.03% as compared to the neat PSf. It signifies that the GO-SiO_2 addition to the membrane was successful, as depicted by the new recorded Si element and higher oxygen composition. Tiny amount of copper (Cu and CuO) was observed in the PSf/GO-SiO_2 membrane with an oxide composition of 0.02%. It can be promoted by the CuO impurities that usually contained in SiO_2 powders [46,47]. However, the content of CuO is not significant and can be neglected to cause the negative impacts on the performance of GO-SiO_2 composite in the membrane. The elemental distribution of GO-SiO_2 on the PSf/GO-SiO_2 membrane is shown in Fig. 3. It can be seen that the distribution of hydrophilic elementals such as O and Si is considerably uniform across the membrane's surface. This can be due to the applied ultrasonic bath homogenization of the dope solution prior to membrane casting. The better dispersibility of oxygenated or hydrophilic groups can provide the desirable membrane performance. Moreover, the rich oxygen content can boost the surface hydrophilicity of the membrane that can provide better permeability.

3.1.2. Pore properties of fabricated membranes

Table 2 provides the estimated thickness, porosity, and pore size of the fabricated membranes. On the thickness parameter, it can be seen that the addition of GO and SiO_2 nanoparticles caused an increase in membrane thickness from 70.32 ± 0.12 μm on neat PSf to 79.55 ± 0.13 μm on PSf/GO/SiO_2 membrane. Similarly, the fabricated membranes' porosities gradually increased as the GO, and SiO_2 nanoparticles were added. A low value of porosity shows the denser membrane, while the higher porosity indicates the existence of abundant void spaces in the membrane's body. The neat PSf membrane has a porosity of 65.10 ± 0.22% and became 72.14 ± 0.46% after the addition of GO and SiO_2 nanoparticles on the PSf/GO/SiO_2 membrane. This phenomenon is in agreement with the SEM results, particularly in the results of cross-section morphology of the membranes that have a visually more well-arranged finger-like structure. The finger-like structure on PSf/GO/SiO_2 membrane is more well-arranged than the neat PSf membrane that causing the more extensive formation of porosity on the body of the membrane. This increase in porosity can enhance the sorption of water, membrane affinity, and permeability of the membrane. Additionally, the pore size of the fabricated membranes was measured to show the effect of GO and SiO_2 addition on this particular parameter. The pore size slightly decreased by the addition of GO and SiO_2 nanoparticles, which was from 43.76 ± 1.12 nm for the neat PSf membrane to 30.45 ± 1.15 nm for the PSf/GO/SiO_2 membrane. The lowest value of pore size was 28.19 ± 0.72 nm for PSf/SiO_2 membrane. Theoretically, the bigger pore size produces higher permeability but lower selectivity [48]. Membranes with smaller pore sizes can achieve better pollutant removal efficiency by filtration, and the permeate flux quality can meet the desired product specification. According to the pore size, all membranes can be classified into the ultrafiltration (UF) membrane since their average pore sizes still fall in the range of 10–100 nm.

Table 2
Thickness, porosity, and pore size of the fabricated membranes.

Membranes	Thickness (μm)	Porosity (%)	Average pore size (nm)
Neat PSf	70.32 ± 0.12	65.10 ± 0.22	43.76 ± 1.12
PSf/GO	72.41 ± 0.10	68.23 ± 0.28	35.14 ± 0.86
PSf/SiO_2	78.23 ± 0.18	63.76 ± 0.24	28.19 ± 0.72
PSf/GO/SiO_2	79.55 ± 0.13	72.14 ± 0.46	30.45 ± 1.15

3.1.3. FTIR analysis

The FTIR analysis was applied to show the new chemical functional groups of the fabricated membranes as the effect of GO and SiO_2 nanoparticles addition. Fig. 4 represents the FTIR spectra of pure SiO_2, GO, neat PSf, PSf/GO, PSf/SiO_2, and PSf/GO/SiO_2 membranes. Pure SiO_2 shows a significant peak at 1078 cm^{-1} corresponds to the presence of Si–O–Si bond [21]. In the pure GO spectrum, it can be seen that the broad peak around 3400-3300 cm^{-1} can be assigned as the *O*–H stretching vibration. It signifies that the GO sample contains abundant amounts of *O*–H groups. The FTIR spectra of all membranes have a similarity in their patterns that indicate these membranes are contained the same polymer backbone, which is polysulfone. The peaks consistently signify the typical pattern of the chemical groups on polysulfone,

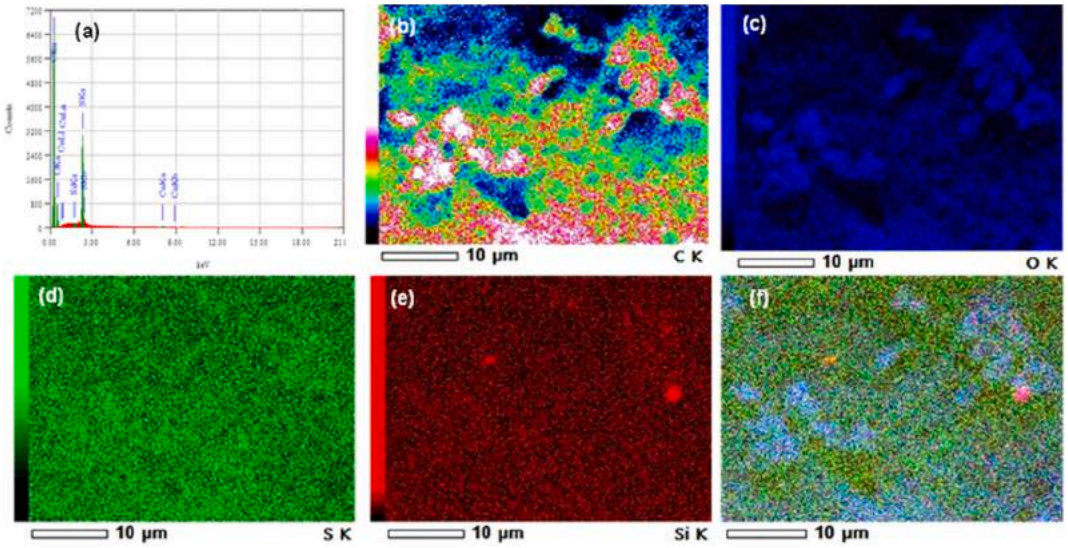

Fig. 3. EDX mapping results of PSf/GO-SiO_2 membrane: (a) EDX spectra, (b) C distribution, (c) O distribution, (d) S distribution, (e) Si distribution, and (f) the overlay plot of C, O, S, and Si distribution.

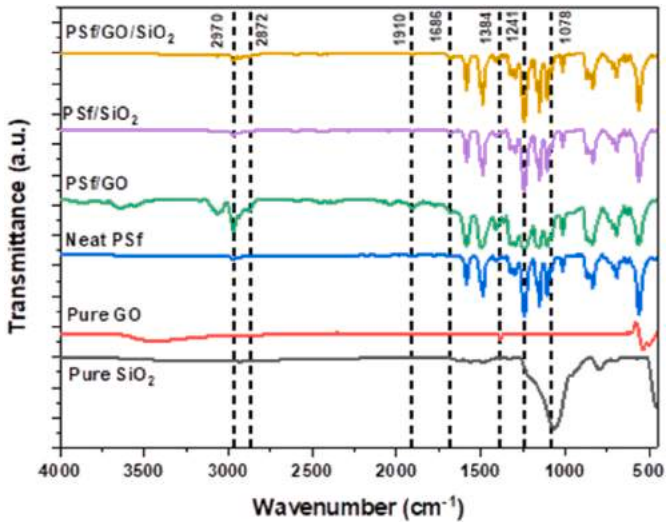

Fig. 4. FTIR spectra of pure SiO_2, GO, neat PSf, PSf/GO, PSf/SiO_2, and PSf/GO/SiO_2 membranes.

such as the peaks at 1241 cm^{-1} are indicated as stretching and absorbance peaks of O═S═O groups [21]. At the same time, a peak at 1157 cm^{-1} belongs to aromatic C═C groups of polysulfone backbone. Moreover, C–H groups were also found by the signal peak on 2970 and 2872 cm^{-1}, which are noticeable on PSf/GO and PSf/GO/SiO_2 membranes. This can be the effect of the C–H groups from GO has successfully embedded on the membranes, resulting in the peak signals at a wavenumber of 2970 and 2872 cm^{-1} [17]. The small peaks at 1910 cm^{-1} and 1686 cm^{-1} are assigned as the existence of C═O and –OH groups that can be contributed from the GO layers [21]. While a tiny distinct peak at 1078 cm^{-1} on PSf/SiO_2 and PSf/GO/SiO_2 corresponds to the existence of Si–O–Si groups from SiO_2. The Si–O–Si groups has the polar properties which can enhance the membrane's hydrophilicity Hence, the presence of chemical functional groups from GO and SiO_2 nanoparticles can contribute to increasing the amounts of hydrophilic sites on the membrane's surface which can provide higher membrane wettability.

3.1.4. XRD analysis

The properties of the crystalline phase of the fabricated membranes were assigned using XRD analysis. This analysis was essential to evidence the presence of GO and SiO_2 nanoparticles in the fabricated membranes. Fig. 5 represents the XRD diffractograms of nano SiO_2, neat PSf, PSf/SiO_2, and PSf/GO/SiO_2 membranes. All membranes show a broad peak at a diffraction angle of 15–20° as the typical diffraction pattern of polysulfone [49]. The diffractogram of the neat PSf membrane did not exhibit any sharp peaks, which indicated that the structure of the membrane was amorphous. The SiO_2 nanoparticles displayed several distinct peaks, of which two peaks with high intensity existed at 2θ of 21° and 26°. GO shows a distinct peak at 11° as the characteristic peak of GO [21]. PSf/GO membrane exhibit some tiny peaks at 11°, 30°, and 38° indicating the embedded GO. Similarly, PSf/SiO_2 membrane presents some peaks at 26°, 42°, and 57° suggesting existence of SiO_2 crystallites. PSf/GO/SiO_2 shows some small distinct peaks at 26°, and 40° that correspond to the presence of SiO_2, while a peak at 38° suggesting the embedded GO. As can be seen, a unique peak of SiO_2 nanoparticles in the PSf/GO/SiO_2 membrane shifted to 37° and 40°, which indicated that the SiO_2 nanoparticles were embedded in the membrane matrix mixture. This shift might be affected by the hydration of SiO_2 nanoparticles during the membrane preparation process [50,51]. Therefore, it can be concluded that GO and SiO_2 were successfully embedded in the PSf/GO/SiO_2 membrane.

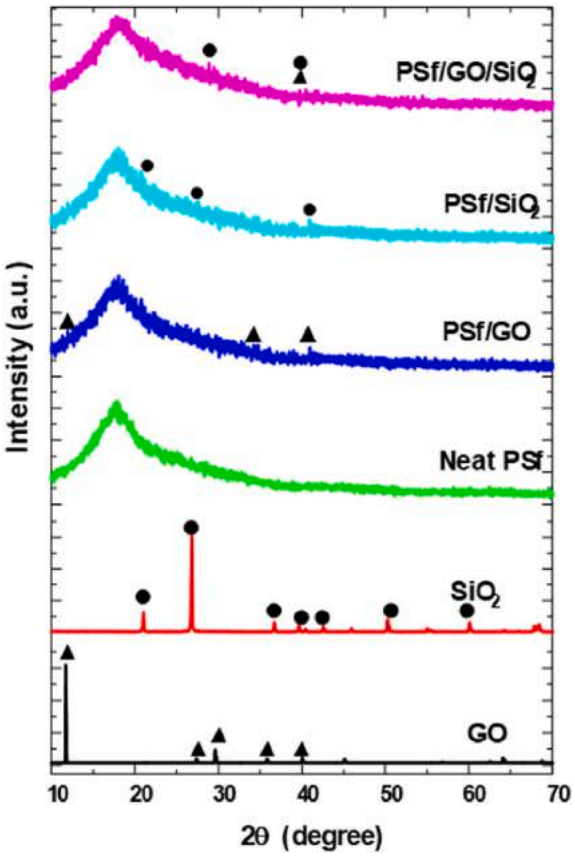

Fig. 5. XRD diffractograms of SiO_2, GO, neat PSf, PSf/SiO_2, and PSf/GO/SiO_2 membranes.

3.1.5. DRS analysis

The photocatalytic activity of the added nanoparticles into the membranes was checked through the UV–vis diffuse reflectance spectrometry analysis (DRS). Fig. 6(a) shows the results of DRS analysis, precisely the absorbance response of GO, SiO_2, and GO/SiO_2 nanoparticles to the light spectra ranging from UV to visible light region with a wavelength of 250–700 nm. This figure also shows the bandgap energy estimations by referring to the Tauc plot method [43]. Based on Fig. 6 (a), it can be seen that SiO_2 showed the unnoticeable difference in the range of light spectra of 250–700 nm. It can be due to the immense nature bandgap energy of SiO_2, so it is photo-catalytically active for light spectrum with a shorter wavelength, which makes no detectable difference in this measurement. On the other hand, the GO nanoparticles possessed a significant change of absorbance, which has a highly dynamic characteristic under the UV light region. The GO nanoparticles were not photo-catalytically active under the visible light region. Interestingly, the mixture of GO/SiO_2 nanoparticles showed a pretty remarkable interaction in the UV light spectrum. The addition of GO remarkably improved the optical properties of SiO_2 to be more active under the UV light spectrum, even with a longer wavelength (250–400 nm). This phenomenon can be due to the impact of GO addition that can reduce the large bandgap energy of SiO_2 by facilitating a fancy electron transfer to prevent the photo-induced electron/hole recombination, which makes the GO/SiO_2 becoming more active even at UV light longer wavelength region. Furthermore, the bandgap energy estimation results show that SiO_2 nanoparticle has undetected bandgap energy from this estimation. Some reported works mentioned that pristine SiO_2 has a bandgap energy >5.00 eV [42,43]. The GO nanoparticle was measured that has a bandgap energy value of 2.91 eV. This value is in a similar range with other reported works [52–54]. The GO/SiO_2 composite has a bandgap energy value of 3.25 eV. In this study, the UV lamp with a

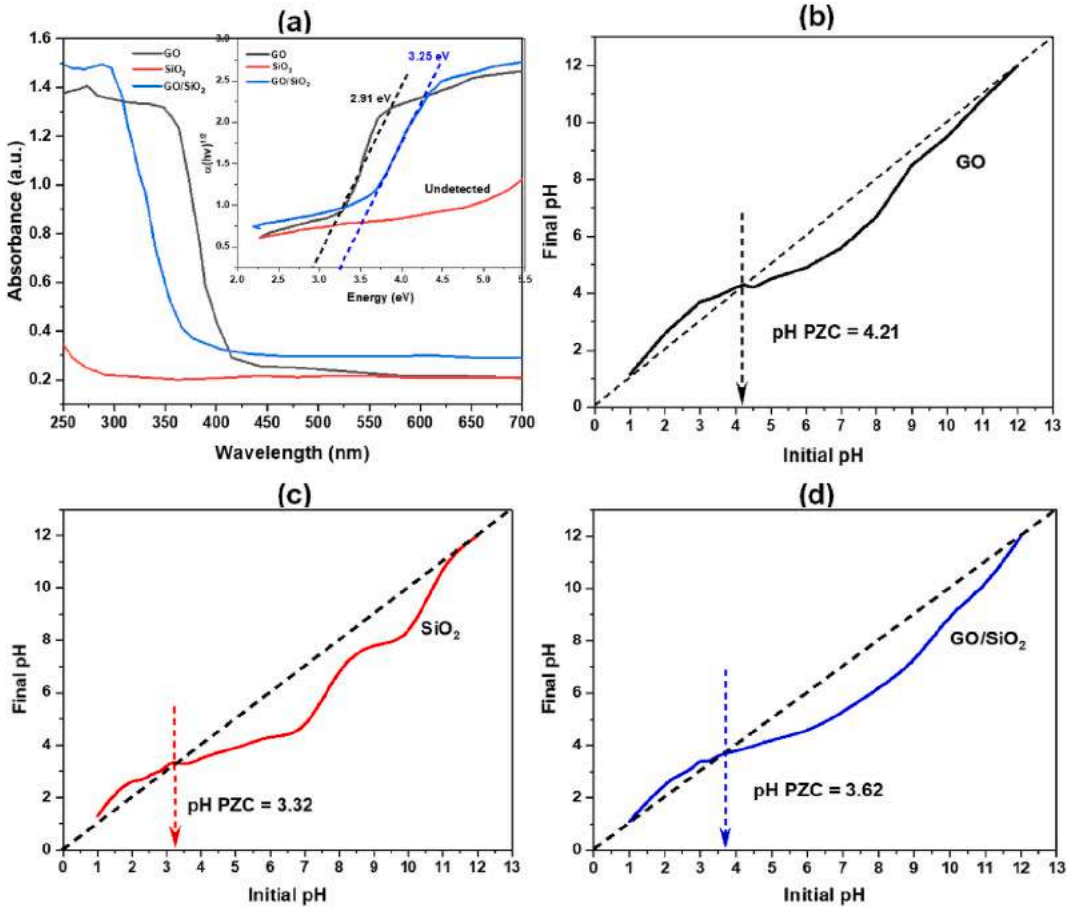

Fig. 6. (a) DRS analysis results contain the interaction of GO, SiO_2, and GO/SiO_2 nanoparticles on UV–vis light and the bandgap energy estimations. PZC analysis results of the tested samples, i.e., (b) GO, (c) SiO_2, and (d) GO/SiO_2.

wavelength of 265 nm was used, it can generate the photon energy value of approximately 4.48 eV, which is higher than the required bandgap energy of the photocatalyst; therefore, it can provide the minimum energy for the photocatalysts to perfectly perform the photocatalytic process on the membrane's surface.

3.1.6. PZC analysis

The surface charge of material plays an essential role in the separation process, especially in membrane processes, in which the membrane's surface takes control of its overall performance. The addition of nanoparticles into the membrane causes some changes in membrane properties such as hydrophilicity, chemical composition, and surface charge. Therefore, in this study, the surface charge of the nanoparticles that indeed have effects on the surface charge of the membrane was evaluated using point of zero charge (PZC) analysis. Fig. 6 (b)–(d) show the results of PZC analysis of GO, SiO_2, and GO/SiO_2, respectively. From those images, it can be seen that the intersections of the curves that indicate the pH_{PZC} values for GO, SiO_2, and GO/SiO_2 were 4.21, 3.32, and 3.62, respectively. All pH_{PZC} values were in the range of 3.32–4.21, which means they have a similar surface charge from the similar surface acidity. When the pH_{PZC} is lower than 7, that means the sample has an acidic surface [55]. The acidic surface tends to have a net negative charge on the surface. On the other hand, when the pH_{PZC} is higher than 7, that means the sample has a basic surface that tends to have a net positively charged surface. It can be stated that all samples, i.e., GO, SiO_2, and GO/SiO_2, have the same negatively charged surface. It signifies that these nanoparticles attributed the fabricated nanohybrid membranes with the negatively charged surface. Consequently, due to the basic pH condition of NRW that was 8.23 ± 0.32, which is higher than the pH_{PZC} of whether GO, SiO_2, and GO/SiO_2, the membrane surface can develop whether a strong adsorption performance against the positively charged pollutant molecules and/or strong repulsion forces against the negatively charged pollutants. These mechanisms can be advantageous for the pollutant rejection performance of the fabricated membranes. Additionally, from the photocatalytic aspects, the photo-induced holes from the photocatalysts' heterojunction process have a strong tendency to react with the water molecules on the negatively charged membrane's surface that can produce large amounts of hydroxyl radicals that are so much helpful for pollutant degradations [56]. Therefore, the embedding GO/SiO_2 nanoparticles on the membrane surface not only carries the photocatalytic properties but also attributed the membrane's surface with negative charges that are extremely useful in pollutant removal performance.

3.1.7. Mechanical strength analysis

The mechanical strength of the fabricated membranes in terms of tensile strength and elongation at break was evaluated, as the results are represented in Fig. 7(a). Based on Fig. 7(a), it can be observed that the tensile strength and elongation at break vary with the addition of different nanoparticles. The neat PSf membrane has a tensile strength of 4.72 ± 0.21 MPa and an elongation at break of 13.00 ± 0.90%. The GO nanoparticles loading on the PSf/GO membrane caused a slight decrease in tensile strength to be 4.50 ± 0.13 MPa and 9.50 ± 0.52% on elongation at break. Similarly, the addition of SiO_2 nanoparticles also showed a decrease in mechanical strength, which was 3.92 ± 0.15 MPa on tensile strength and 8.50 ± 0.43% on elongation at break. The incorporation of GO and SiO_2 on PSf/GO/SiO_2 membrane attributed the values of tensile strength of 3.55 ± 0.18 MPa and elongation at break of

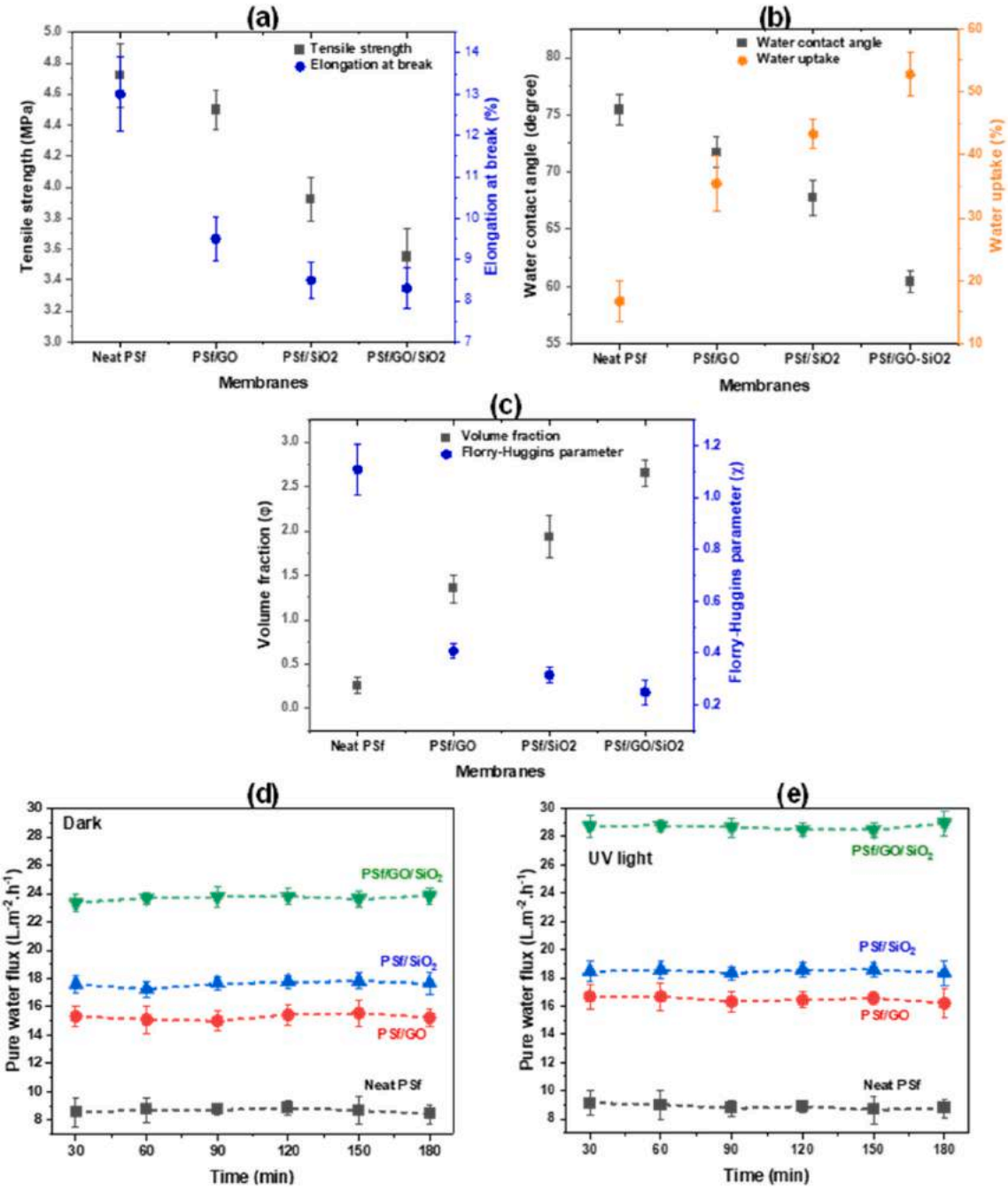

Fig. 7. Membrane properties: (a) Tensile strength and elongation at break, (b) Water contact angle and water uptake ability, (c) Membrane's affinity including volume fraction and Flory-Huggins interaction parameter, and Pure water flux (PWF): (d) dark and (e) UV light conditions.

8.30 ± 0.53%. It indicates that the nanoparticle addition into the membrane caused a reduction in the mechanical strength of the membranes. This might be caused by the creation of gaps between polymer matrix as a consequence of the addition of nanoparticles. Additionally, based on the XRD results, the embedded nanoparticles on the polymer matrix made some crystallite attachments that resulted in an increase in the crystallinity index of the membranes, especially with the addition of SiO_2 nanoparticles. With the more created gaps and the increase of crystalline structures in the membrane's body, the polymer matrix becomes less elastic and becomes more brittle so that the mechanical strength decreases. Some previous works recommended not to introduce the nanoparticles more than 2 %-wt because it resulted in not only mechanical strength decrease but also the un-uniform nanoparticle distribution due to the agglomeration of nanoparticles [2,57]. Fortunately, the mechanical strength reductions were not that bad; the PSf/GO/SiO_2 experienced approximately 24.78% reduction in tensile strength and 36.15% reduction in elongation at break as compared to the neat PSf membrane. The applied pressure on filtration was 5 bar (~0.5 MPa), which is still below the tensile strength of the membranes; therefore, these membranes can still be used for the filtration process, and their mechanical properties are acceptable.

3.1.8. Membrane's hydrophilicity, water uptake ability, and affinity analyses

The membrane's hydrophilicity is another crucial characteristic that should be examined to understand the surface characteristic. Water contact angle has a correlation with water uptake ability or often known as water sorption characteristic. Fig. 7(b) shows the results of water

contact angle and water uptake ability of the fabricated membranes. The measured water contact angles were 75.42° ± 1.32°, 71.69° ± 1.27°, 67.75° ± 1.51°, and 60.34° ± 0.97° for neat PSf, PSf/GO, PSf/SiO_2, and PSf/GO/SiO_2 membranes, respectively. The neat PSf has the highest water contact angle, which means this membrane possesses the lowest hydrophilicity among the others. PSf/GO/SiO_2 membrane, on the other hand, shows the lowest value of water contact angle, which corresponds with the highest surface hydrophilicity. The higher hydrophilicity of the membrane surface means the stronger attraction to water molecules might be generated, which subsequently resulted in higher permeate flux and lower fouling tendency. Interestingly, this finding is in accordance with the results of the water uptake ability of the fabricated membranes. The measured values of water uptake ability were 16.76 ± 3.21%, 35.42 ± 4.35%, 43.27 ± 2.32%, and 52.78 ± 3.45% for neat PSf, PSf/GO, PSf/SiO_2, and PSf/GO/SiO_2 membranes, respectively. It can be explained that the addition of GO and SiO_2 nanoparticles into the membrane attached the new functional groups with polar characteristics such as –OH and C═O, and the crystallite of SiO_2 across the membrane's surface resulted in higher attraction forces to the water molecules. The addition of GO and SiO_2 nanoparticles also developed a higher porosity in the membrane, which can be quickly filled with water. As a result, the synergetic effects of the hydrophilic surface and porous structure make the PSf/GO/SiO_2 membrane possess the lowest contact angle and the highest water uptake ability.

The membrane's affinity towards water molecules was studied by adopting the theoretical model of Flory-Huggins (FH) [58]. This model can be applied to know deeper about the sorption behavior of water into the matrix of the membrane. Fig. 7(c) depicts the results of the membrane's affinity study in terms of volume fraction and FH interaction parameter. The estimated volume fractions (φ) were 0.26 ± 0.09, 1.35 ± 0.15, 1.93 ± 0.23, and 2.65 ± 0.14 for neat PSf, PSf/GO, PSf/SiO_2, PSf/GO/SiO_2 membranes, respectively. The FH parameter (χ) value can be written as an inversed logarithmic form of volume fraction. The calculated FH interaction parameters were 1.11 ± 0.10, 0.41 ± 0.03, 0.31 ± 0.03, and 0.25 ± 0.05 for neat PSf, PSf/GO, PSf/SiO_2, PSf/GO/SiO_2 membranes, respectively. These FH parameters can be used to explain the affinity between the membrane and water molecules. The lower value of the FH parameter indicates the higher sorption of water ability [58]. The higher sorption of water can be leading to performance improvements on flux, pollutant rejection, and antifouling potential. The addition of GO and SiO_2 nanoparticles on the PSf/GO/-SiO_2 membrane resulted in the lowest value of the FH interaction parameter among the other membranes, suggesting that the membrane ability after the addition of GO and SiO_2 nanoparticles can improve the membrane performance in a positive way.

The initial check of the photocatalytic properties on the membrane performance was carried out using a method of pure water flux (PWF) determination. The filtration experiments using pure water (DI water) for 180 min were conducted in the dark and under UV light to be compared. Fig. 7(d and e) represent the results of PWF in dark and under UV light exposure for the fabricated membranes. It can be observed that the addition of GO and SiO_2 nanoparticles increased the PWF value in both dark and UV light conditions. The average values of PWF on dark condition were 8.67 ± 0.75, 15.28 ± 0.77, 17.62 ± 0.62, and 23.67 ± 0.58 L m^{-2} h^{-1} for neat PSf, PSf/GO, PSf/SiO_2, and PSf/GO/SiO_2 membranes, respectively. While the measured values of PWF under UV light condition were 8.86 ± 0.85, 16.48 ± 0.76, 18.45 ± 0.58, and 28.68 ± 0.63 L m^{-2} h^{-1} for neat PSf, PSf/GO, PSf/SiO_2, and PSf/GO/SiO_2 membranes, respectively. These findings indicate that the UV light exposure caused a significant impact on the membranes embedded with a photo-catalytically active particle which are PSf/GO and PSf/GO/SiO_2, as suggested from the DRS results. The PWF improvement in membranes with embedded photocatalysts is caused by the increase of hydrophilicity during UV light irradiation [59]. In the photocatalyst, the photo-induced holes can oxidize the superoxide radicals and creating the oxygen vacancies [60]. These oxygen vacancies tend to attract water molecules and generating adsorbed hydroxyl (OH) groups, thus enhances the surface hydrophilicity. The higher surface hydrophilicity led to provide stronger attraction force to water molecules [61], which resulting in an improved PWF. The PSf/GO/SiO_2 experienced about a 22.19% increase in PWF compared to dark conditions. Therefore, these results signify that the embedded GO and SiO_2 can perform the photocatalytic process under UV light irradiation on the surface of PSf/GO/-SiO_2 membrane that provided an improvement in PWF and might also be enhancing pollutant removal and antifouling potential.

3.2. Effect of GO addition on membrane performance

The effects of GO addition with various concentrations in PSf/GO membranes were evaluated by measuring the permeate flux and pollutant rejection using an actual sample of NRW. The experiment was conducted using a membrane filtration with an operating pressure of 5 bar for 5 h. The results of the filtration experiment in terms of permeate flux and pollutant rejection on PSf/GO membranes are presented in Figs. S3(a) and (b), respectively. From Fig. S3(a), it can be seen that the neat PSf membrane experienced the lowest permeate flux among the other membranes. Significant improvement on permeate flux occurred when the GO was added. For example, the initial permeate flux of neat PSf was 9.85 L m^{-2} h^{-1}, and after the addition of 0.5%-wt of GO, the initial permeate flux increased to 10.55 L m^{-2} h^{-1}. Moreover, increasing the GO addition into the membrane resulted in a higher permeate flux. The addition of 1.5 %-wt of GO generated an initial permeate flux of 12.54 L m^{-2} h^{-1} and also can maintain 71.61% of permeate flux after going through a 5 h duration of filtration. This improvement after GO addition can be due to the higher hydrophilicity of the membrane's surface were gained with the addition of a higher amount of GO nanoparticles. As reflected from contact angle results, the addition of GO nanoparticles exhibited the lower contact angle and higher water uptake ability meaning that the GO addition significantly improved the surface hydrophilicity. The improved surface hydrophilicity supported the higher permeate flux.

Another evaluated parameter, as shown in Fig. S3(b), is the pollutant rejection performance. In this study, the evaluated pollutant parameters were focused on COD and NH_3–N removals. Based on the results, it can be seen that the neat PSf achieved the pollutant removals of 45.66 ± 2.31% for COD and 25.43 ± 1.22% for NH_3–N. The addition of GO nanoparticles also significantly improved the pollutant removal performance. By adding 0.5 %-wt GO, the pollutant removals were 55.32 ± 1.33% for COD and 32.54 ± 1.67% for NH_3–N, which considerably improved 21.15% on COD removal and 27.95% on NH_3–N removal. The higher concentration of GO in the membrane resulted in the higher removals performance. The addition of 1.5 %-wt of GO presented the best concentration in the membrane that improved the pollutant removals to be 68.75 ± 1.43% for COD removal and 55.43 ± 2.12% for NH_3–N removal. The improvements in pollutant removal after the GO nanoparticle addition can be due to the electrostatic field formation on the membrane's surface caused by the embedded GO nanoparticles. This condition creates a polar surface that is supported by the new functional groups attached so that they can provide the massive attraction forces to water molecules that have a similar polarity and repel the organic contaminants, which are mostly nonpolar substances. Hence, the higher addition of GO nanoparticles resulted in more abundant polar sites for the PSf/GO membrane's surface, which improved the pollutant rejection. It is also worth noting that the uncontrolled addition of nanoparticles can create entirely different results because the addition with more than 2 %-wt of the nanoparticle can cause aggregation, bigger pore, and un-uniform properties, as reported in previous studies [62]. Therefore, based on the results of this study, the addition of GO nanoparticles by 1.5 %-wt was considered as the best concentration that significantly enhanced the permeate flux and pollutant rejection of the membrane.

3.3. Effect of SiO_2 addition on membrane performance

The incorporation of SiO_2 nanoparticles with various concentrations was observed to know the effects of SiO_2 concentration in permeate flux and pollutant removal efficiency. Fig. S3(c) shows the results of SiO_2 concentration effects on permeate flux. It can be seen that the SiO_2 nanoparticle introduction into the membrane raised the permeate flux value compared to the neat PSf membrane. The addition of 0.5 %-wt SiO_2 nanoparticles generated an initial permeate flux of 11.72 L m^{-2} h^{-1}, while the neat PSf membrane generated only 9.85 L m^{-2} h^{-1} on permeate flux. This permeate flux was also higher than the PSf/GO membrane with the same addition of 0.5 %-wt of nanoparticles. It can be due to the fact that the embedded SiO_2 nanoparticles provided a higher membrane's hydrophilicity and membrane's affinity towards which resulted in higher permeate flux. The addition of higher SiO_2 nanoparticles tends to increase the permeate flux gradually. PSf/SiO_2 membrane with 1.5 %-wt of SiO_2 concentration appeared as the best formulation for achieving the highest permeate flux among the other membranes with an initial value of 13.21 L m^{-2} h^{-1}. This 1.5 %-wt SiO_2 concentration also provided a relatively more stable permeate flux compared to the other concentrations. Once again, the surface hydrophilicity might be played a vital role in this phenomenon that prevents the fouling formation and can maintain a better permeate flux profile. Fig. S3(d) presents the pollutant rejection values of the fabricated membranes using various SiO_2 nanoparticle concentrations. The addition of SiO_2 nanoparticles remarkably improved the rejections of COD and NH_3–N from the NRW. The loading of 0.5 %-wt of SiO_2 nanoparticle can increase the membrane's removal ability from 45.66 ± 2.31% to 55.32 ± 1.76% for COD, and from 25.43 ± 1.22% to 32.54 ± 2.19% for NH_3–N. The higher concentration of SiO_2 addition generated a positive trend in pollutant removals. The addition of 1.5 %-wt showed as the best formulation that resulted in the highest COD and NH_3–N removals with values of 68.75 ± 1.87% and 56.11 ± 2.03%, respectively. It is also found that the membrane can better remove COD than NH_3–N. This is explainable by the relative molecular size of COD and NH_3–N, which of COD is a parameter to show the natural organic matters in NRW sample, which have a relatively larger size of molecules compared to NH_3–N. Since the pore size of the PSf/SiO_2 membrane is 1.86 ± 0.33 nm, which can effectively remove the organic matters such as proteins, lipids, and carbohydrates. In contrast, the NH_3–N can ionize in water and form an ionic reaction ($NH_3 + H_2O \leftrightarrow NH_4^+ + OH^-$), in which the products are soluble in water and appear in tiny size of ions. The membrane possesses more struggle in the removal of ionic compounds rather than the organic compounds; therefore, the membrane provided better COD rejection than NH_3–N rejection during the observation.

3.4. Effects of combined GO/SiO_2 nanoparticles addition and UV light exposure during filtration on the fabricated membrane's performance

The photo-filtration experiment was applied. In this method, the membrane module was irradiated using a UV lamp as the source of energy to initiate the photocatalytic activity on the membrane surface to assess the membrane's performance after attributed the photocatalytic properties from the addition of GO/SiO_2 nanoparticles. The conventional filtration was also carried out in a dark condition as a control variable. Fig. 8 shows the complete results of permeate flux and pollutant rejection of fabricated membranes under UV light exposure and dark condition of filtrations. Fig. 8(a) presents the results of neat PSf membrane, the permeate flux profile of the dark condition and under UV light filtrations did not show any significant difference. Also, the pollutant rejection of using the neat PSf membrane did not show a significant improvement, as reflected in Fig. 8(e). This clearly signifies that the neat PSf membrane has no photocatalytic activity. In contrast, after the addition of GO and/or SiO_2 nanoparticles into the membranes, the membranes' performance presented quite remarkable improvements. As shown in Fig. 8(b), PSf/GO membrane possessed a different profile on permeate flux in the dark and under UV light exposure. In the dark condition, PSf/GO membrane exhibited an initial permeate flux of 12.54 L m^{-2} h^{-1}, while under UV light exposure filtration, it reached an initial permeate flux of 14.32 L m^{-2} h^{-1}. Similarly, the pollutant rejection also improved when the filtration was conducted under UV light exposure, as shown in Fig. 8(f). These findings are in agreement with the DRS results that the GO nanoparticle has a good interaction with light spectra in the UV light region and possesses bandgap energy of 2.91 eV to perform the photocatalytic process. Another finding, the addition of SiO_2 nanoparticles, exhibited slight improvements in permeate flux and pollutant rejection as reflected in Fig. 8(c) and (h), respectively.

The addition of both GO and SiO_2 nanoparticles showed great improvements in permeate flux and pollutant rejection, as the results are depicted in Fig. 8(d) and (h), respectively. By using PSf/GO/SiO_2 membrane on conventional filtration condition, the initial permeate flux raised from 9.85 L m^{-2} h^{-1} (neat PSf membrane) to 17.87 L m^{-2} h^{-1} with 73.22 ± 1.16% of COD removal and 78.54 ± 0.83% of NH_3–N removal. Moreover, there were extensive improvements when the membrane filtration was conducted under UV light irradiation. It is

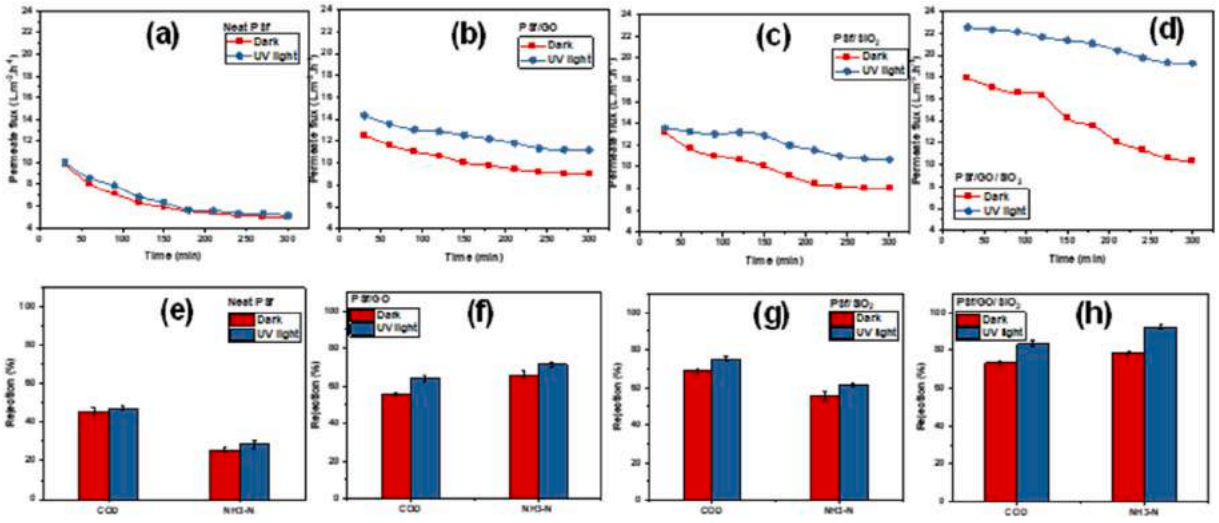

Fig. 8. The results of membranes' performance in terms of permeate flux: (a) neat PSf, (b) PSf/GO, (c) PSf/SiO_2, (d) PSf/GO/SiO_2, and pollutant rejection using: (e) neat PSf, (f) PSf/GO, (g) PSf/SiO_2, (h) PSf/GO/SiO_2, using filtration in a dark condition and under UV light exposure.

found that the permeate flux significantly increased by 26.55% compared to in the dark condition. The UV light irradiation can also stabilize the permeate flux nicely, with a permeate flux of 22.55 L m^{-2} h^{-1} at the initial and 19.25 L m^{-2} h^{-1} at the end of 5 h of filtration, which means it can remarkably maintain the permeate flux by 85.36%. It is worth to note that the incorporation of GO and SiO_2 nanoparticles not only provide better permeate flux performance in the filtration under UV exposure but also improves the permeate flux in conventional filtration conditions (dark), as the results are shown in Fig. 8. The modified membranes with photocatalysts have higher permeate flux in both dark and under UV light conditions and also maintained stable flux performance. These phenomena can be promoted for three main reasons. First, the increase of hydrophilicity due to the addition of GO and SiO_2 nanoparticles, thereby increasing the attraction towards water molecules that resulted in higher permeate flux [64]. Second, the high membrane porosity generated after the addition of photocatalysts that created a larger effective filtration area and adsorbed more water inside the pore structure resulted in an increase in permeability. Third, the photocatalytic process can degrade the concentrated pollutants on the membrane's surface so that the pollutants do not deposit on the membrane's surface, and the filtration process might not be disturbed.

The pollutant rejections also improved when the membrane was operated under the UV light condition. The pollutant rejection efficiency also showed significant enhancements with this UV light-assisted filtration. In fact, COD removal increased from 73.22 ± 1.28% to 83.55 ± 2.57% and NH_3–N removal improved from 78.54 ± 3.12% to 92.41 ± 1.87%. The improvements of permeate flux and pollutant rejection using PSf/GO/SiO_2 membrane under this condition can be due to the photocatalytic activity on the GO/SiO_2 nanoparticles sites on the membrane's surface. UV irradiation initiated the excitation of electrons from the valence band to the conduction band of the nanoparticle that further created electron and hole sites. The electron and hole migrated according to heterojunction pattern and generated the redox reaction, which generated radical molecules that can be in the forms of superoxide ($\cdot O_2^-$) and hydroxyl ($\cdot$OH) radicals [63]. These radicals are so reactive, they can easily react with pollutant molecules, and the pollutants are degraded to smaller and less hazardous substances such as carbon dioxide (CO_2) and nitrogen (N_2) [31]. These mechanisms take place on the membrane's surface, so the concentrated pollutant can be diminished that resulting in a low tendency of fouling and concentration polarization and generating a relatively easier filtration process. This mechanism creates a higher as well as a more stable permeate flux profile. Moreover, by the photocatalytic activity on the membrane's surface, the pollutant removal mechanisms are not limited to the sieving mechanism but also supported by photocatalytic degradation, which significantly improved the pollutant removal performance. Therefore, the incorporation of GO and SiO_2 nanoparticles into PSf membrane and with filtration process under UV light exposure remarkably improved the permeate flux and pollutant removal by creating a synergetic process of filtration and photocatalytic degradation.

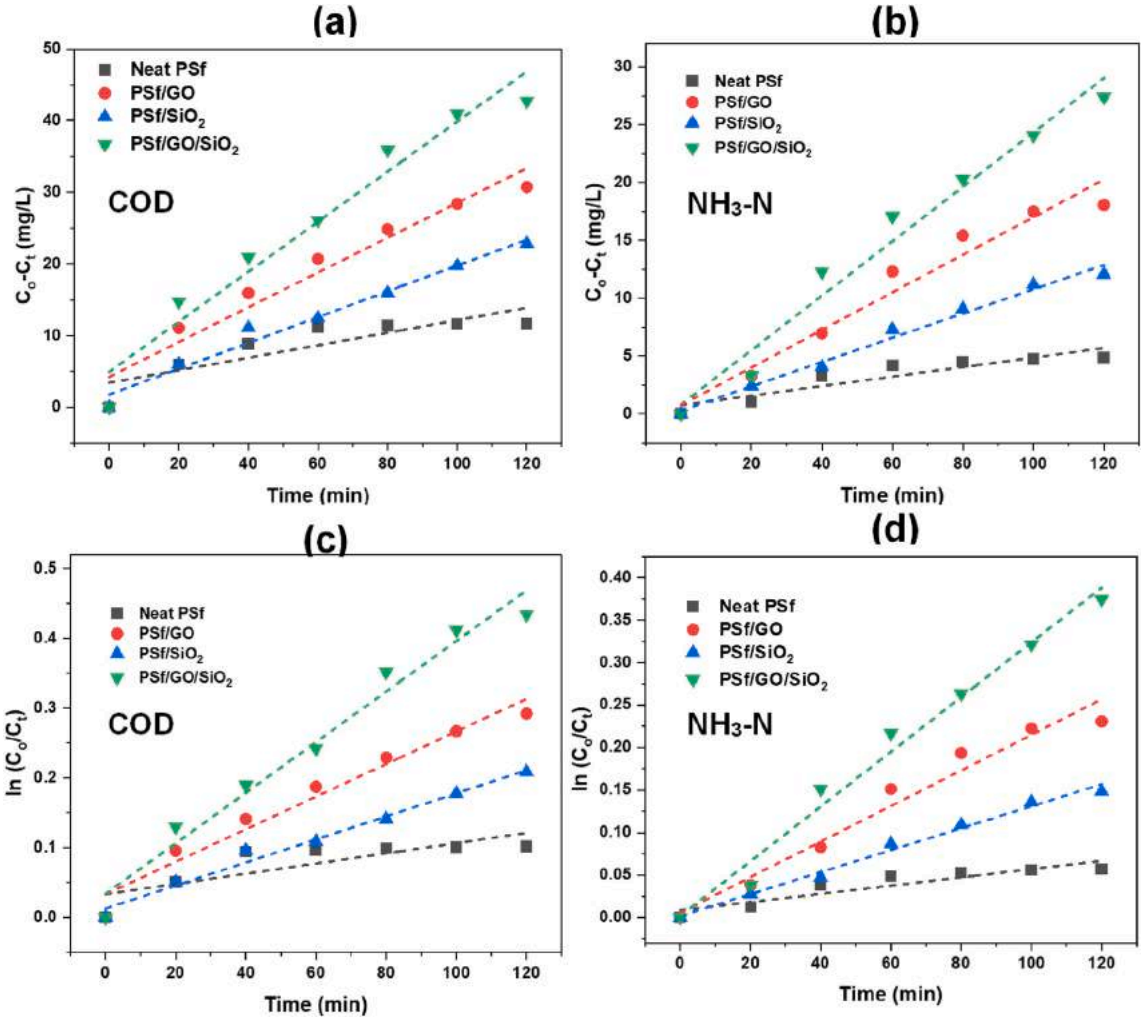

Fig. 9. Zero-order photocatalysis kinetic model fittings for (a) COD removal and (b) NH_3–N removal. Pseudo-first order photocatalysis kinetic model fittings for (c) COD removal and (d) NH_3–N removal.

3.5. Kinetic evaluation on photocatalytic degradation ability of the fabricated membranes

The kinetic behavior of photocatalytic degradation on the fabricated membranes was studied using two kinetic models, namely the zero-order and pseudo-first order models. This observation was evaluated by assessing the COD and NH_3–N degradation rate using the sample of NRW as the feed. The membrane sheet was mounted onto the glass holder and was immersed into the NRW sample. This experiment was carried out in a dark and closed chamber equipped with a UV lamp. Before the UV lamp was turned on, the membrane was immersed for 60 min in order to achieve the adsorption equilibrium state for ensuring that only the photocatalytic process was assayed. Fig. 9 shows the fitting plots of photocatalytic degradation on COD and NH_3–N by applying the zero-order and pseudo-first order kinetic models, whereas the fitted parameters are summarized in Table S3. Based on the results, it can be observed that PSf/GO/SiO_2 membrane possessed the higher rate constants k_0 (0.3492 mg/L min for COD removal and 0.2352 mg/L min for NH_3–N removal) and k_1 (0.0036 min^{-1} for COD removal and 0.0032 min^{-1} for NH_3–N removal) in both of applied kinetic models. It signifies that PSf/GO/SiO_2 membrane has a better photocatalytic activity that can faster degrade the pollutants with higher removal ability than the other membranes in the same condition [2]. Furthermore, the pseudo-first order kinetic showed a relatively better fit to model the photocatalytic degradation using PSf/GO/SiO_2 membrane compared to the zero-order kinetic model. It is reflected by the values of the coefficient of determination (R^2). In COD removal, the values of R^2 are 0.9462 for the zero-order model and 0.9729 for the pseudo-first order model. Corroboratively, in NH_3–N removal, the values are 0.9722 for the zero-order model and 0.9841 for the pseudo-first order model. Therefore, these findings suggest that the pseudo-first order kinetic model better described the COD and NH_3–N removal using photocatalytic degradation provided by PSf/GO/SiO_2 membrane.

In common heterogeneous photocatalytic degradation, reactive species including holes, superoxide, and hydroxyl radicals are the main substances to degrade the pollutants. In this study, trapping tests were performed to further investigate the relevance, existence, and relative activity of the reactive species on pollutant degradations. Oxalic acid, benzoquinone, and methanol were used as the scavengers for holes, superoxide, and hydroxyl radicals, respectively [64]. Fig. 10 depicts the effect of scavengers on COD and NH_3–N degradations using PSf/GO, PSf/SiO_2, and PSf/GO/SiO_2 membranes. It can be observed that the scavengers reduce the photo-degradation efficiency on all membranes. This means that the scavengers disrupt the active species to react with pollutants. The relative order of active species' effects on photocatalytic degradation can be ordered as $h^+ > \cdot O_2^- > \cdot OH$. It is also found that all active species play important roles in pollutant degradation, by eliminating one of them resulted in reduction of degradation efficiency. The proposed mechanisms of pollutant degradation by the PSf/GO/SiO_2 membrane under UV light irradiation are written in Eq. 18–24 [65].

Photo-induced electrons and holes generations:

$$GO/SiO_2 + hv \rightarrow GO/SiO_2(e^- + h^+) \quad (18)$$

$$e^- + h^+ \rightarrow \text{heat} \quad (19)$$

Radical formations:

$$O_2 + e^- \rightarrow \cdot O_2^- \quad (20)$$

$$H_2O + h^+ \rightarrow H^+ + \cdot OH \quad (21)$$

$$OH^- + h^+ \rightarrow \cdot OH \quad (22)$$

Pollutant degradations:

$$\text{Pollutants} + \cdot O_2^- \rightarrow \text{degraded products} \quad (23)$$

$$\text{Pollutants} + \cdot OH \rightarrow \text{degraded products} \quad (24)$$

3.6. The photocatalysts and the membranes photocatalytic stability, resistance during filtration, and antifouling potential evaluations

The photocatalytic activity of the photocatalysts and fabricated membrane were investigated. Fig. S4 shows the photocatalytic stability of the nanoparticles in the suspension system on the COD and NH_3–N removals. It can be seen that GO, SiO_2, and GO/SiO_2 nanoparticles have a distinctive difference in the photodegradation abilities. GO/SiO2 nanoparticle appears as the most powerful photocatalyst among the others. Overall, the photodegradation ability of the photocatalysts seems to have higher pollutant removal ability compared to the membranes as depicted in Fig. 11. The neat PSf membrane experienced unnoticeable removal performance in both COD and NH_3–N parameters. It is undoubtedly due to the neat PSf membrane was not a photocatalytic material as suggested by DRS results. In contrast, the other three membranes showed quite remarkable photocatalytic degradation activities after the addition of GO and SiO_2 nanoparticles. The PSf/GO membrane nanoparticles performed a better removal performance than the PSf/SiO_2 membrane, which can be caused by the lower bandgap energy level of GO than SiO_2. This lower bandgap resulted in ease to conduct the photocatalysis process on the PSf/GO membrane [52]. Interestingly, by the addition of GO and SiO_2 nanoparticles on the PSf/GO/SiO_2 membrane, the photocatalytic performance improved significantly and became the highest performance among the other membranes. The synergetic effect of GO and SiO_2 nanoparticles can create the active photocatalytic sites, which attributed bandgap energy of 3.25 eV and also the active surface charge that possessed a pH_{PZC} value of 3.62. The simultaneous photocatalytic process and surface charge properties resulted in an enhancement of COD and NH_3–N removal.

To further examine the durability of the membranes, a five

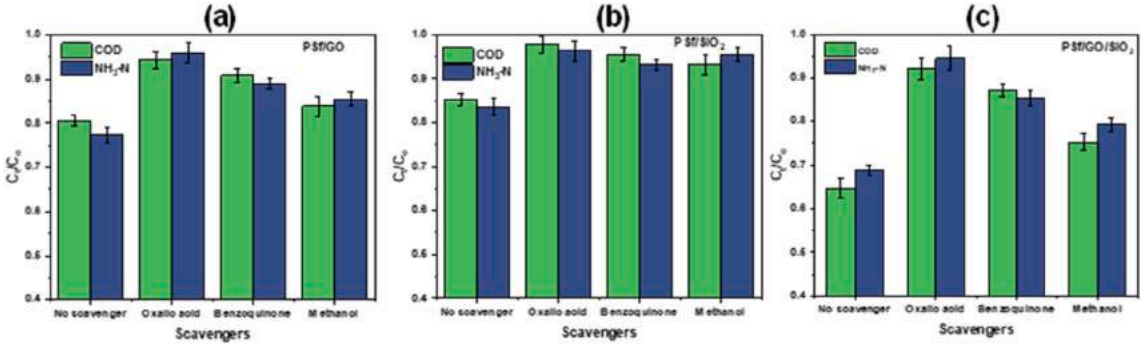

Fig. 10. Trapping test results using oxalic acid, benzoquinone, and methanol to quench hole, superoxide, and hydroxyl radicals, respectively for (a) PSf/GO, (b) PSf/SiO_2, and (c) PSf/GO/SiO_2 membranes.

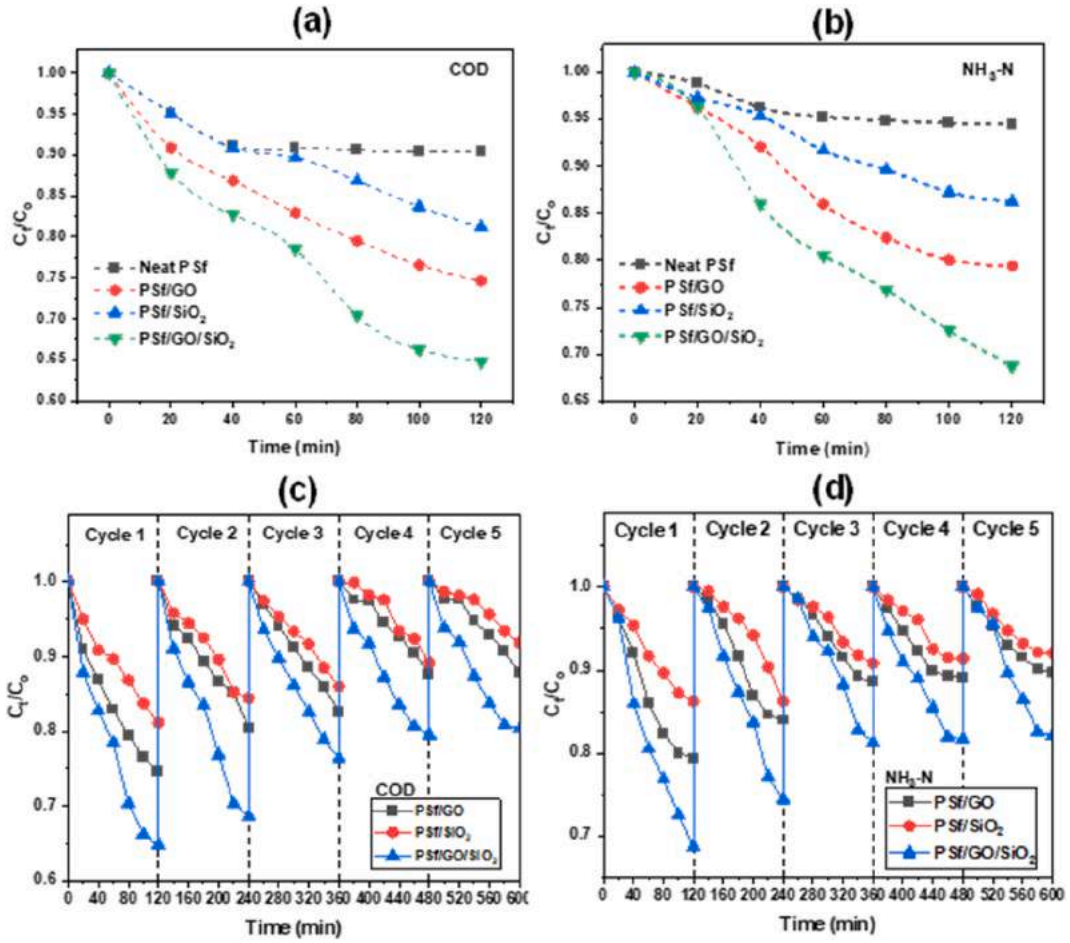

Fig. 11. Profile of pollutant removal by the photocatalytic process for (a) COD and (b) NH_3–N. The cycle test results of photocatalytic performance of PSf/GO, PSf/SiO_2, and PSf/GO/SiO_2 membranes for (c) COD removal and (d) NH_3–N removal.

consecutive photocatalytic cycles test was conducted for PSf/GO, PSf/SiO_2, and PSf/GO/SiO_2 membranes. Fig. 11(c) and (d) represent the cycle test results on COD and NH_3–N removals, respectively. Based on the results, PSf/GO/SiO_2 membrane exhibited the most prominent performance, retrievability, and stability of photocatalytic properties among the other membranes. It can also be found that the photocatalytic degradation efficiency experienced a gradual reduction after the cycle was changed. For example, in the PSf/GO/SiO_2 membrane profile, the COD and NH_3–N removals were 35.39% and 31.27%, respectively. At the end of the third cycle, COD and NH_3–N removals were 23.63% and 18.71%, respectively. And, at the end of the last (fifth) cycle, COD and NH_3–N removals were 19.47% and 18.05%, respectively These efficiency reductions can occur due to the loss of some active photocatalytic sites on the membrane surface during the cycle changing and washing-cleaning process. By looking at it holistically, the photocatalytic activity reduction was not so extreme, which was reflected by the fact that even at the third cycle, the membrane can still proceed with the photocatalytic degradation process. It suggests that the PSf/GO/SiO_2 membrane has an excellent photocatalytic property and also has pretty remarkable durability that can possibly be used for a more extended period of time.

Table 3 provides the resistances during filtration of the fabricated membranes in the dark and under the UV light irradiation on the filtration experiments. These calculations take into account all the occurred fouling types, including the internal resistance (R_m), adsorptive fouling (R_a), deposition fouling (R_d), and concentration polarization (R_{cp}). From the results, it is found that the addition of nanoparticles causes a reduction in all resistances. In conventional filtration conditions, the addition of SiO_2 nanoparticles into the membrane showed a slightly better performance compared to GO nanoparticle addition in reducing the resistance during filtration. Contrary, in the filtration under UV light exposure, a reverse phenomenon is found. The addition of GO nanoparticles resulted in a more significant reduction in membrane resistance compared to SiO_2 nanoparticles addition. It is explainable due to the photocatalytic property of GO that can be activated under the presence of UV light with lower bandgap energy,

Table 3
Comparison of membrane's fouling resistances, i.e., internal resistance (R_m), adsorptive fouling resistance (R_a), deposition fouling resistance (R_d), and concentration polarization resistance (R_{cp}) during filtration at dark and under UV light irradiation conditions.

Membranes	R_m (m^{-1} x 10^{12})	R_a (m^{-1} x 10^{12})	R_d (m^{-1} x 10^{12})	R_{cp} (m^{-1} x 10^{12})
Dark condition				
Neat PSf	11.54 ± 0.61	8.75 ± 0.14	12.87 ± 0.32	7.83 ± 0.53
PSf/GO	10.12 ± 0.24	7.76 ± 0.18	11.04 ± 0.18	7.11 ± 0.27
PSf/SiO_2	9.86 ± 0.17	8.33 ± 0.21	9.65 ± 0.21	5.87 ± 0.34
PSf/GO/SiO_2	7.32 ± 0.21	5.67 ± 0.16	7.65 ± 0.25	4.38 ± 0.33
Under UV light irradiation				
Neat PSf	11.38 ± 0.27	8.86 ± 0.33	11.86 ± 0.19	7.66 ± 0.18
PSf/GO	7.12 ± 0.11	4.32 ± 0.29	7.90 ± 0.24	4.15 ± 0.26
PSf/SiO_2	8.98 ± 0.19	7.04 ± 0.13	8.71 ± 0.21	4.69 ± 0.33
PSf/GO/SiO_2	5.02 ± 0.26	1.43 ± 0.24	3.21 ± 0.24	1.45 ± 0.23

whereas SiO_2 possessed too high bandgap energy that caused just a slight improvement. Furthermore, the PSf/GO/SiO_2 membrane exhibited the most favorable performance on fouling reduction that occurred both in the dark and under UV light filtration conditions. The membrane hydrophilicity plays a more dominant action in the dark filtration, while the photocatalytic property acts as a vital role in the photo-filtration under UV light for fouling prevention. In fact, the PSf/GO/SiO_2 membrane attributed the highest hydrophilicity and also photocatalytic property that are reflected from contact angle and DRS analyses, respectively. These characteristics made the PSf/GO/SiO_2 membrane can perform an exquisite performance whether in conventional or under UV light filtration conditions.

Fig. 12 presents the further results of fouling observations to explain the effects of nanoparticle addition and filtration condition on the fouling reduction and flux recovery ratio. Fig. 12(a) shows the ratios of total resistance (R_T), irreversible resistance (R_{Ir}), reversible resistance (R_R), and flux recovery ratio (FRR) of the fabricated membranes in the dark filtration condition. Generally, it can be seen that the higher fouling ratios occurred, resulting in the lower FRR value, as in accordance with other studies. It can be found that the R_T values were 58.12 ± 2.40%, 46.32 ± 3.28%, 51.34 ± 2.91%, and 43.65 ± 2.57% for neat PSf, PSf/GO, PSf/SiO_2, and PSf/GO/SiO_2 membranes, respectively, whereas the FRR values were 32.17 ± 2.54%, 54.33 ± 1.23%, 52.65 ± 1.85%, and 57.66 ± 1.90% neat PSf, PSf/GO, PSf/SiO_2, and PSf/GO/SiO_2 membranes, respectively. The PSf/GO/SiO_2 membrane possessed the lowest fouling with the highest FRR value among the other membranes. Further improvements of the PSf/GO/SiO_2 membrane were achieved when the UV light irradiation was carried out in the filtration condition. The total resistance decreased from 43.65 ± 2.57% to 25.43 ± 2.81% with improved FRR value from 57.66 ± 1.90% in the dark condition to 69.21 ± 2.76% under UV light exposure. As shown in Table S4, it can be seen that the membrane porosity significantly decreased after being used in the dark filtration, while the porosity reduction in membrane after UV light exposure filtration can be relatively maintained. It can be promoted by the fouling reduction especially the pore blocking. The reduction in fouling tendency can be due to the photocatalytic degradation of pollutants on the membrane surface that can prevent fouling formation and concentration polarization. Fig. 12(c)–(e) depict the images of the membranes' surfaces after filtrations with different conditions. Based on Fig. 12(c), the neat PSf membrane shows the worst fouling formation that indicates this fouling was responsible the low values of permeate flux and stability of the neat PSf membrane. The addition of GO and SiO_2 nanoparticle remarkably reduced the foulant formation compared to the neat PSf membrane, as the image is shown in Fig. 12(d). Further fouling reduction was shown by the PSf/GO/SiO_2 membrane when it was conducted under UV light exposure that resulted in visually decreased on foulant formation compared to the other membranes as can be seen in Fig. 12(e). The reduced fouling tendency exhibited the easier water transport passing through the membrane film and resulting in the higher FRR value [27].

The integrated filtration and photodegradation on a single membrane were successfully improved the membrane performance in terms of permeate flux stability, pollutant rejection, membrane durability, antifouling potential, and flux recovery ability. This integrated process has been applied using numerous types of membrane materials, photocatalysts, and synthesis methods in various kind of contaminants including dyes, organic matters, pharmaceutical products, and surfactants, as summarized in Table 4. Based on all findings, it can be concluded that the addition of GO and SiO_2 nanoparticles into the PSf membrane was so much useful to create not only a hydrophilic membrane with a great affinity towards the water but also a photocatalytic property that significantly improved the membrane characteristics and performance and the findings are comparable with previously reported studies. Finally, this PSf/GO/SiO_2 nanohybrid membrane that was performed under the UV light irradiation filtration condition showed a promising potential of advanced treatment for natural rubber-laden wastewater.

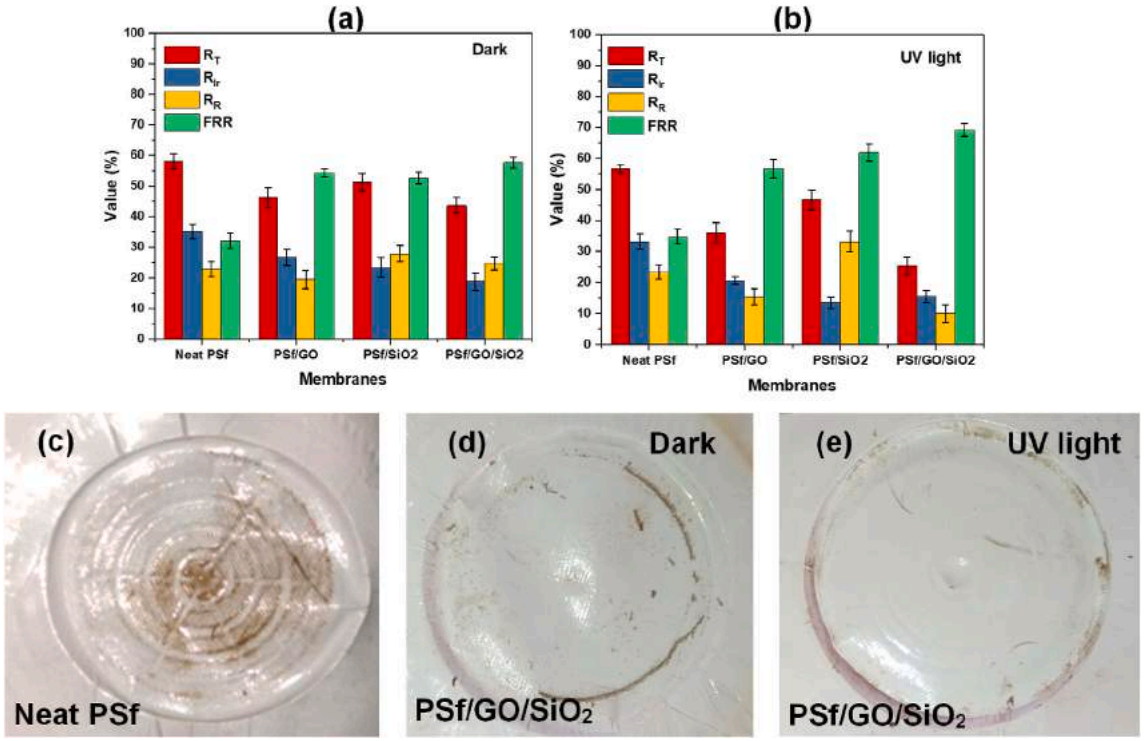

Fig. 12. The results of the antifouling potential of the fabricated membranes using filtration conditions of (a) Dark and (b) Under UV light irradiation. The images of the membranes after filtration (c) neat PSf membrane, (d) PSf/GO/SiO_2 membrane in the dark filtration, and (e) PSf/GO/SiO_2 membrane under UV light irradiation filtration condition.

Table 4
Comparison of the photocatalytic membrane composite based on membrane material, photocatalyst, synthesis method, tested pollutant, and the findings with previously reported studies.

Membrane material	Photocatalyst	Synthesis method	Tested pollutant	Findings	Ref.
PVDF + PP	TiO_2	Blending	4-nitrophenol (4-NP)	50% removal efficiency of 4-NP after 5 h of irradiation. The 4-NP concentration in permeate was equal in retentate.	[66]
TiO_2/Al_2O_3 ceramic membrane	TiO_2/Al_2O_3	Sol-gel	Direct Black 168	Dye removal of 82%. The membranes photocatalytic properties helped in permeate flux improvement and prevented fouling formation.	[67]
SiO_2/TiO_2 ceramic membrane	SiO_2/TiO_2	Sol gel	Sodium dodecylbenzene sulfonate (SDBS)	SDBS removal of 89% after 100 min of process. The addition of photocatalyst into membrane enhanced permeate flux and reduced fouling.	[68]
PSf	TiO_2-GO	Blending	Methylene blue (MB)	The composite membrane exhibited 3–4 times faster in dye removal under UV and sunlight. Composite addition increased the membranes hydrophilicity.	[69]
PVDF	LiCl–TiO_2	Blending	Natural organic matter (NOM)	The photocatalyst addition improved the hydrophilicity and pollutant rejection. The composite membranes exhibited a self-cleaning ability.	[70]
Bi_2WO_6 ceramic membrane	Reduced graphene oxide (rGO)	Coating	Ciprofloxacin	The composite membrane has a good fouling control and exhibited 59.95% in ciprofloxacin removal under visible light for 7.5 h.	[38]
PSf	WO_3	Blending	COD removal from dairy wastewater	PSf/WO3 membrane showed a high COD removal and stable permeate flux. It also exhibited a low irreversible fouling and attributed a self-cleaning property.	[34]
Anodic aluminum oxide (AAO)	ZnO nanosheets	Coating	*E. coli* bacteria	Under UV light irradiation, the membrane showed a 70% removal of *E. coli*. The membrane also attributed self-antifouling ability.	[35]
PSf	Cu_2O	Blending	Ibuprofen	Under visible light condition, the membrane can remove 86% of ibuprofen with a rate of 32.6×10^{-3} min^{-1}. It also developed the antifouling ability.	[36]
PES	Oxygen doped graphite-C_3N_4	Blending	Phenol	The composite membrane showed an enhanced photocatalytic ability with better fouling prevention. Under UV light irradiation, it improved 35.78% higher phenol removal compared to the conventional filtration condition.	[37]
PSf	GO/SiO_2	Blending	Natural rubber-laden wastewater	Under UV light exposure, PSf/GO/SiO_2 membrane showed COD removal increased from 73 to 84%, and NH_3–N removal improved from 78 to 92%. It maintained 85.4% of flux stability and prevented fouling formation.	This study

4. Conclusion

This work has investigated the effects of GO and SiO_2 nanoparticles in the PSf membrane to perform an integrated photocatalytic and membrane filtration for treatment of natural rubber-laden wastewater (NRW). SEM tests show that the surface micromorphology of PSf/GO/SiO_2 membrane possessed a uniform dispersion of nanoparticles, and its cross-section characteristic were attributed to the asymmetric membrane morphology with a well-arranged finger-like structure. The new oxygenated groups such as –OH and C═O from GO were found in the FTIR spectra of the membrane after incorporating GO into the detected crystallite structure of SiO_2 with an average size of 23.47 nm and 31.87% of the distribution. DRS results showed that GO/SiO_2 composite successfully enhanced the photocatalytic activity and possessed a bandgap energy of 3.25 eV, which made the SiO_2 to be active under UV light exposure after the addition of GO nanoparticles. GO and SiO_2 nanoparticles addition improved the surface charge of the membrane that had an acidic surface with a pH_{PZC} of 3.62. The addition of nanoparticles into the membrane decreased mechanical strength due to the gap formations that weakened the polymer chains of the membrane. Conducting filtration under UV irradiation using PSf/GO/SiO_2 membrane exhibited a remarkable improvement in permeate flux by 129% from 9.85 L m^{-2} h^{-1} to 22.55 L m^{-2} h^{-1} and maintained 85.4% of permeate flux stability. With respect to removal performance, under the photo-filtration process, chemical oxygen demand (COD) removal increased from 73 to 84%, and ammonia-nitrogen (NH_3–N) removal improved from 78 to 92%. The photocatalytic kinetic evaluation suggested that the pseudo-first order kinetic model had a better fit than the zero-order kinetic. Regeneration tests showed that the PSf/GO/SiO_2 membrane has outstanding durability. The resistance during filtration and antifouling potential evaluations revealed that the GO/SiO_2 composite under UV light irradiation during filtration remarkably reduced the fouling formation and generated a high flux recovery ratio. This implies that this PSf/GO/SiO_2 composite is promising for an effective treatment of NRW.

CRediT author contribution statement

Tutuk Djoko Kusworo: Resources, Methodology, Conceptualization, Validation, Writing-review and editing. Andri Cahyo Kumoro: Review-Editing. Nita Aryanti: Data analysis, Validation. Dani Puji Utomo: Collecting data, Formal analysis. Hasrinah Hasbullah: Formal analysis, Writing-review editing. Fadhilah Fatma Lingga: Investigation, Collecting data, Writing-original draft. Ade Widiastuti: Investigation, Collecting data, Writing-original draft. Monica Yulfarida: Writing-original draft, Collecting data. Febio Dalanta: Data curation, Formal analysis, Visualization, Writing-review editing. Tonni Agustiono Kurniawan: Data analysis and Writing-review editing.

Declaration of competing interest

The authors declare that they have no known competing financial interests or personal relationships that could have appeared to influence the work reported in this paper.

Acknowledgment

The authors acknowledged Institute for Research and Community Services (LPPM), Diponegoro University. This research was fully funded by Diponegoro University World-Class Research Grant (WCR-UNDIP) No.118-31/UN7.6.1/PP/2021. The authors would also thank the PTPN VII in Bengkulu, Indonesia, for providing the samples of natural rubber-laden wastewater for this study.

Appendix A. Supplementary data

Supplementary data to this article can be found online at https://doi.org/10.1016/j.memsci.2022.120663.

References

[1] D. Tanikawa, T. Kataoka, Y. Hirakata, M. Hatamoto, T. Yamaguchi, Pre-treatment and post-treatment systems for enhancing natural rubber industrial wastewater

treatment, Process Saf. Environ. Protect. 138 (2020) 256–262, https://doi.org/10.1016/J.PSEP.2020.03.030.
[2] T.D. Kusworo, N. Ariyanti, D.P. Utomo, Effect of nano-TiO2 loading in polysulfone membranes on the removal of pollutant following natural-rubber wastewater treatment, J. Water Proc. Eng. 35 (2020), 101190, https://doi.org/10.1016/j.jwpe.2020.101190.
[3] N. Habashi, N. Mehrdadi, A. Mennerich, A. Alighardashi, A. Torabian, Hydrodynamic cavitation as a novel approach for pretreatment of oily wastewater for anaerobic co-digestion with waste activated sludge, Ultrason. Sonochem. 31 (2016) 362–370, https://doi.org/10.1016/J.ULTSONCH.2016.01.022.
[4] C. Zhao, J. Zhou, Y. Yan, L. Yang, G. Xing, H. Li, P. Wu, M. Wang, H. Zheng, Application of coagulation/flocculation in oily wastewater treatment: a review, Sci. Total Environ. 765 (2021), 142795, https://doi.org/10.1016/J.SCITOTENV.2020.142795.
[5] S. Vinardell, S. Astals, M. Peces, M.A. Cardete, I. Fernández, J. Mata-Alvarez, J. Dosta, Advances in anaerobic membrane bioreactor technology for municipal wastewater treatment: a 2020 updated review, Renew. Sustain. Energy Rev. 130 (2020), 109936, https://doi.org/10.1016/J.RSER.2020.109936.
[6] D. Hu, K. Luo, H. Ma, H. Min, Y. Zhao, Y. Cui, S. Wang, N. Ning, L. Zhang, W. Liu, A sustainability anti-infective pharmaceutical wastewater treatment technology: multi-stage vertical variable diameter membrane bioreactor with DO online controlling, Bioresour. Technol. 311 (2020), 123507, https://doi.org/10.1016/J.BIORTECH.2020.123507.
[7] S.A. Younis, H.A. Maitlo, J. Lee, K.H. Kim, Nanotechnology-based sorption and membrane technologies for the treatment of petroleum-based pollutants in natural ecosystems and wastewater streams, Adv. Colloid Interface Sci. 275 (2020), 102071, https://doi.org/10.1016/J.CIS.2019.102071.
[8] P. Das, S. Dutta, K.K. Singh, Insights into membrane Crystallization: a sustainable tool for value added product recovery from effluent streams, Separ. Purif. Technol. (2020), 117666, https://doi.org/10.1016/j.seppur.2020.117666.
[9] X. Liu, S. Zhao, X. Zhang, W. Jia, Z. Zou, Q. Wang, Application of sodium alginate as a coagulant aid for mitigating membrane fouling induced by humic acid in dead-end ultrafiltration process, Separ. Purif. Technol. 253 (2020), 117421, https://doi.org/10.1016/J.SEPPUR.2020.117421.
[10] E. Evdochenko, J. Kamp, R. Dunkel, V.v. Nikonenko, M. Wessling, Charge distribution in polyelectrolyte multilayer nanofiltration membranes affects ion separation and scaling propensity, J. Membr. Sci. 636 (2021), 119533, https://doi.org/10.1016/J.MEMSCI.2021.119533.
[11] D. Wanke, A. da Silva, C. Costa, Modification of PVDF hydrophobic microfiltration membrane with a layer of electrospun fibers of PVP-co-PMMA: increased fouling resistance, Chem. Eng. Res. Des. 171 (2021) 268–276, https://doi.org/10.1016/J.CHERD.2021.05.004.
[12] A. Vaysizadeh, A.A. Zinatizadeh, S. Zinadini, Fouling mitigation and enhanced dye rejection in UF and NF membranes via layer-by-layer (LBL) assembly and altering PVP percentage as pore former, Environ. Technol. Innovat. 23 (2021), 101698, https://doi.org/10.1016/J.ETI.2021.101698.
[13] C. Wang, X. Song, Y. Liu, C. Zhang, PVC-g-PVP amphiphilic polymer synthesis by ATRP and its membrane separation performance for silicone-containing wastewater, Polymer 229 (2021), 123965, https://doi.org/10.1016/J.POLYMER.2021.123965.
[14] Y. Liu, J. Wang, Y. Wang, H. Zhu, X. Xu, T. Liu, Y. Hu, High-flux robust PSf-b-PEG nanofiltration membrane for the precise separation of dyes and salts, Chem. Eng. J. 405 (2021), 127051, https://doi.org/10.1016/J.CEJ.2020.127051.
[15] V.H. Nguyen, Q.B. Tran, X.C. Nguyen, L.T. Hai, T.T.T. Ho, M. Shokouhimehr, D.V. N. Vo, S.S. Lam, H.P. Nguyen, C.T. Hoang, Q.V. Ly, W. Peng, S.Y. Kim, T. van Tung, Q. van Le, Submerged photocatalytic membrane reactor with suspended and immobilized N-doped TiO2 under visible irradiation for diclofenac removal from wastewater, Process Saf. Environ. Protect. 142 (2020) 229–237, https://doi.org/10.1016/J.PSEP.2020.05.041.
[16] V. Vatanpour, G.N. Nekouhi, M. Esmaeili, Preparation, characterization and performance evaluation of ZnO deposited polyethylene ultrafiltration membranes for dye and protein separation, J. Taiwan Inst. Chem. Eng. 114 (2020) 153–167, https://doi.org/10.1016/J.JTICE.2020.09.008.
[17] G. Fan, C. Chen, X. Chen, Z. Li, S. Bao, J. Luo, D. Tang, Z. Yan, Enhancing the antifouling and rejection properties of PVDF membrane by Ag3PO4-GO modification, Sci. Total Environ. 801 (2021), 149611, https://doi.org/10.1016/J.SCITOTENV.2021.149611.
[18] P.v. Chai, J.Y. Law, E. Mahmoudi, A.W. Mohammad, Development of iron oxide decorated graphene oxide (Fe3O4/GO) PSf mixed-matrix membrane for enhanced antifouling behavior, J. Water Proc. Eng. 38 (2020), 101673, https://doi.org/10.1016/J.JWPE.2020.101673.
[19] K. Rambabu, G. Bharath, A.F. Arangadi, S. Velu, F. Banat, P.L. Show, ZrO2 incorporated polysulfone anion exchange membranes for fuel cell applications, Int. J. Hydrogen Energy 45 (2020) 29668–29680, https://doi.org/10.1016/J.IJHYDENE.2020.08.175.
[20] S. Anisah, M. Kanezashi, H. Nagasawa, T. Tsuru, Al2O3 nanofiltration membranes fabricated from nanofiber sols: preparation, characterization, and performance, J. Membr. Sci. 611 (2020), 118401, https://doi.org/10.1016/J.MEMSCI.2020.118401.
[21] H. Wu, B. Tang, P. Wu, Development of novel SiO2–GO nanohybrid/polysulfone membrane with enhanced performance, J. Membr. Sci. 451 (2014) 94–102, https://doi.org/10.1016/J.MEMSCI.2013.09.018.
[22] T.D. Kusworo, F. Dalanta, N. Aryanti, N.H. Othman, Intensifying separation and antifouling performance of PSf membrane incorporated by GO and ZnO nanoparticles for petroleum refinery wastewater treatment, J. Water Proc. Eng. 41 (2021), 102030, https://doi.org/10.1016/J.JWPE.2021.102030.
[23] H.G. Lemos, R.A. Ragio, A.C.S. Conceição, E.C. Venancio, J.C. Mierzwa, E.L. Subtil, Assessment of mixed matrix membranes (MMMs) incorporated with graphene oxide (GO) for co-treatment of wastewater and landfill leachate (LFL) in a membrane bioreactor (MBR), Chem. Eng. J. 425 (2021), 131772, https://doi.org/10.1016/J.CEJ.2021.131772.
[24] M.L. Tran, C.C. Fu, L.Y. Chiang, C. te Hsieh, S.H. Liu, R.S. Juang, Immobilization of TiO2 and TiO2-GO hybrids onto the surface of acrylic acid-grafted polymeric membranes for pollutant removal: analysis of photocatalytic activity, J. Environ. Chem. Eng. 8 (2020), 104422, https://doi.org/10.1016/J.JECE.2020.104422.
[25] F. Kazemi, Y. Jafarzadeh, S. Masoumi, M. Rostamizadeh, Oil-in-water emulsion separation by PVC membranes embedded with GO-ZnO nanoparticles, J. Environ. Chem. Eng. 9 (2021), 104992, https://doi.org/10.1016/J.JECE.2020.104992.
[26] I. Ratman, T.D. Kusworo, D.P. Utomo, D.A. Azizah, W.A. Ayodyasena, Petroleum refinery wastewater treatment using three steps modified nanohybrid membrane coupled with ozonation as integrated pre-treatment, J. Environ. Chem. Eng. 8 (2020), 103978, https://doi.org/10.1016/J.JECE.2020.103978.
[27] H. Younas, Y. Zhou, X. Li, X. Li, Q. Sun, Z. Cui, Z. Wang, Fabrication of high flux and fouling resistant membrane: a unique hydrophilic blend of polyvinylidene fluoride/polyethylene glycol/polymethyl methacrylate, Polymer 179 (2019), 121593, https://doi.org/10.1016/J.POLYMER.2019.121593.
[28] X. Wang, S. Li, P. Chen, F. Li, X. Hu, T. Hua, Photocatalytic and antifouling properties of TiO2-based photocatalytic membranes, Mater. Today Chem. 23 (2022), 100650, https://doi.org/10.1016/J.MTCHEM.2021.100650.
[29] Z. Balta, E.B. Simsek, Insights into the photocatalytic behavior of carbon-rich shungite-based WO3/TiO2 catalysts for enhanced dye and pharmaceutical degradation, N. Carbon Mater. 35 (2020) 371–383, https://doi.org/10.1016/S1872-5805(20)60495-4.
[30] B. Li, M. Meng, Y. Cui, Y. Wu, Y. Zhang, H. Dong, Z. Zhu, Y. Feng, C. Wu, Changing conventional blending photocatalytic membranes (BPMs): focus on improving photocatalytic performance of Fe3O4/g-C3N4/PVDF membranes through magnetically induced freezing casting method, Chem. Eng. J. 365 (2019) 405–414, https://doi.org/10.1016/J.CEJ.2019.02.042.
[31] F. Dalanta, T.D. Kusworo, N. Aryanti, N.H. Othman, Optimization of AC/TiO2/CeO2 composite formulation for petroleum refinery wastewater treatment via simultaneous adsorption-photocatalytic process using D-optimal mixture experimental design, J. Environ. Chem. Eng. 9 (2021), 106517, https://doi.org/10.1016/J.JECE.2021.106517.
[32] L.S. Roselin, N. Patel, S.A. Khayyat, Codoped g-C3N4 nanosheet for degradation of organic pollutants from oily wastewater, Appl. Surf. Sci. 494 (2019) 952–958, https://doi.org/10.1016/j.apsusc.2019.07.077.
[33] X. Wang, F. Wang, C. Bo, K. Cheng, J. Wang, J. Zhang, H. Song, Promotion of phenol photodecomposition and the corresponding decomposition mechanism over g-C3N4/TiO2 nanocomposites, Appl. Surf. Sci. 453 (2018) 320–329, https://doi.org/10.1016/J.APSUSC.2018.05.082.
[34] M. Peyravi, M. Jahanshahi, S. Khalili, Fouling of WO3 nanoparticle-incorporated PSf membranes in ultrafiltration of landfill leachate and dairy a combined wastewaters: an investigation using model, Chin. J. Chem. Eng. 25 (2017) 741–751, https://doi.org/10.1016/J.CJCHE.2016.12.001.
[35] B. Najma, A.K. Kasi, J. Khan Kasi, A. Akbar, S.M.A. Bokhari, I.R. Stroe, ZnO/AAO photocatalytic membranes for efficient water disinfection: synthesis, characterization and antibacterial assay, Appl. Surf. Sci. 448 (2018) 104–114, https://doi.org/10.1016/J.APSUSC.2018.04.063.
[36] R. Singh, V.S.K. Yadav, M.K. Purkait, Cu2O photocatalyst modified antifouling polysulfone mixed matrix membrane for ultrafiltration of protein and visible light driven photocatalytic pharmaceutical removal, Separ. Purif. Technol. 212 (2019) 191–204, https://doi.org/10.1016/J.SEPPUR.2018.11.029.
[37] N.E. Salim, N.A.M. Nor, J. Jaafar, A.F. Ismail, M.R. Qtaishat, T. Matsuura, M.H. D. Othman, M.A. Rahman, F. Aziz, N. Yusof, Effects of hydrophilic surface macromolecule modifier loading on PES/O-g-C3N4 hybrid photocatalytic membrane for phenol removal, Appl. Surf. Sci. 465 (2019) 180–191, https://doi.org/10.1016/J.APSUSC.2018.09.161.
[38] Y. Li, L. Zhu, Evaluation of the antifouling and photocatalytic properties of novel poly(vinylidene fluoride) membranes with a reduced graphene oxide–Bi2WO6 active layer, J. Appl. Polym. Sci. 134 (2017), 45426, https://doi.org/10.1002/app.45426.
[39] H. Mahdavi, N. Zeinalipour, M.A. Kerachian, A.A. Heidari, Preparation of high-performance PVDF mixed matrix membranes incorporated with PVDF-g-PMMA copolymer and GO@SiO2 nanoparticles for dye rejection applications, J. Water Proc. Eng. 46 (2022), 102560, https://doi.org/10.1016/j.jwpe.2022.102560.
[40] E. Bonyadi, F.Z. Ashtiani, S. Ghorabi, A.S. Niknejad, Bio-inspired hybrid coating of microporous polyethersulfone membranes by one-step deposition of polydopamine embedded with amino-functionalized SiO2 for high-efficiency oily wastewater treatment, J. Environ. Chem. Eng. 10 (2022), 107121, https://doi.org/10.1016/j.jece.2021.107121.
[41] J. Low, J. Yu, M. Jaroniec, S. Wageh, A.A. Al-Ghamdi, Heterojunction photocatalysts, Adv. Mater. 29 (2017), https://doi.org/10.1002/adma.201601694.
[42] M.M. Motawea, M.A.T. Hussein, M.M. Elsenety, H.M. Ali, T.A. Seaf El-Nasr, H. Gomaa, Mesoporous hierarchical ZrO2@rice straw-derived SiO2 nanocomposite for rapid adsorption and sunlight-driven photocatalytic degradation of methylene blue, J. Photochem. Photobiol. Chem. 426 (2022), 113758, https://doi.org/10.1016/J.JPHOTOCHEM.2021.113758.
[43] Y. Wu, S. Ren, X. Chang, X. Zhang, Investigation of adsorption-photocatalytic synergistic mechanism of globular TiO2–ZrO2–SiO2 composites by a synergy factor, Opt. Mater. 122 (2021), 111723, https://doi.org/10.1016/J.OPTMAT.2021.111723.

[44] T.D. Kusworo, H. Susanto, N. Aryanti, N. Rokhati, I.N. Widiasa, H. Al-Aziz, D. P. Utomo, D. Masithoh, A.C. Kumoro, Preparation and characterization of photocatalytic PSf-TiO2/GO nanohybrid membrane for the degradation of organic contaminants in natural rubber wastewater, J. Environ. Chem. Eng. 9 (2021), 105066, https://doi.org/10.1016/J.JECE.2021.105066.
[45] O.S. Serbanescu, S.I. Voicu, V.K. Thakur, Polysulfone functionalized membranes: properties and challenges, Mater. Today Chem. 17 (2020), 100302, https://doi.org/10.1016/J.MTCHEM.2020.100302.
[46] A. Ohsawa, K. Honda, N. Toyokura, Metal impurities near the SiO2 - Si interface, J. Electrochem. Soc. 131 (1984) 2964–2969, https://doi.org/10.1149/1.2115451.
[47] R. Sreedharan, M. Mohan, S. Saini, A. Roy, K. Bhattacharjee, Intermediate Cu-O-Si phase in the Cu-SiO $_2$/Si(111) system: growth, elemental, and electrical studies, ACS Omega 6 (2021) 23826–23836, https://doi.org/10.1021/acsomega.1c02646.
[48] W.U. Arifeen, M. Kim, J. Choi, K. Yoo, R. Kurniawan, T.J. Ko, Optimization of porosity and tensile strength of electrospun polyacrylonitrile nanofibrous membranes, Mater. Chem. Phys. 229 (2019) 310–318, https://doi.org/10.1016/J.MATCHEMPHYS.2019.03.020.
[49] Y.T. Chung, E. Mahmoudi, A.W. Mohammad, A. Benamor, D. Johnson, N. Hilal, Development of polysulfone-nanohybrid membranes using ZnO-GO composite for enhanced antifouling and antibacterial control, Desalination 402 (2017) 123–132, https://doi.org/10.1016/j.desal.2016.09.030.
[50] S.S. Marzouk, V. Naddeo, F. Banat, S.W. Hasan, Preparation of TiO2/SiO2 ceramic membranes via dip coating for the treatment of produced water, Chemosphere 273 (2021), 129684, https://doi.org/10.1016/J.CHEMOSPHERE.2021.129684.
[51] Y. Zhang, F. Liu, Y. Lu, L. Zhao, L. Song, Investigation of phosphorylated TiO2–SiO2 particles/polysulfone composite membrane for wastewater treatment, Desalination 324 (2013) 118–126, https://doi.org/10.1016/J.DESAL.2013.06.007.
[52] A.A. Elhakim, M. El-Kemary, M.M. Ibrahim, I.M. El-Mehasseb, H.S. El-Sheshtawy, Direct Z-scheme of WO3/GO decorated with silver nanoparticles for synergetic adsorption and photocatalytic activity for organic and inorganic water pollutants removal, Appl. Surf. Sci. 564 (2021), 150410, https://doi.org/10.1016/J.APSUSC.2021.150410.
[53] J. Park, Y. Kim, S.Y. Park, S.J. Sung, H.W. Jang, C.R. Park, Band gap engineering of graphene oxide for ultrasensitive NO2 gas sensing, Carbon N Y 159 (2020) 175–184, https://doi.org/10.1016/j.carbon.2019.11.063.
[54] U.A. Méndez-Romero, S.A. Pérez-García, X. Xu, E. Wang, L. Licea-Jiménez, Functionalized reduced graphene oxide with tunable band gap and good solubility in organic solvents, Carbon N Y 146 (2019) 491–502, https://doi.org/10.1016/j.carbon.2019.02.023.
[55] S. Psaltou, E. Kaprara, K. Triantafyllidis, M. Mitrakas, A. Zouboulis, Heterogeneous catalytic ozonation: the significant contribution of PZC value and wettability of the catalysts, J. Environ. Chem. Eng. 9 (2021), 106173, https://doi.org/10.1016/J.JECE.2021.106173.
[56] J.M. Monteagudo, A. Durán, I. San Martín, P. Carrillo, Effect of sodium persulfate as electron acceptor on antipyrine degradation by solar TiO2 or TiO2/rGO photocatalysis, Chem. Eng. J. 364 (2019) 257–268, https://doi.org/10.1016/J.CEJ.2019.01.165.
[57] T.D. Kusworo, N. Aryanti, F. Dalanta, Effects of incorporating ZnO on characteristic, performance, and antifouling potential of PSf membrane for PRW treatment, IOP Conf. Ser. Mater. Sci. Eng. 1053 (2021), 012134, https://doi.org/10.1088/1757-899x/1053/1/012134.
[58] B.M. Ganesh, A.M. Isloor, A.F. Ismail, Enhanced hydrophilicity and salt rejection study of graphene oxide-polysulfone mixed matrix membrane, Desalination 313 (2013) 199–207, https://doi.org/10.1016/J.DESAL.2012.11.037.
[59] K. Guan, Relationship between photocatalytic activity, hydrophilicity and self-cleaning effect of TiO2/SiO2 films, Surf. Coating. Technol. 191 (2005) 155–160, https://doi.org/10.1016/j.surfcoat.2004.02.022.
[60] Y.C. Lee, Y.P. Hong, H.Y. Lee, H. Kim, Y.J. Jung, K.H. Ko, H.S. Jung, K.S. Hong, Photocatalysis and hydrophilicity of doped TiO2 thin films, J. Colloid Interface Sci. 267 (2003) 127–131, https://doi.org/10.1016/S0021-9797(03)00603-9.
[61] J. Tang, H. Quan, J. Ye, Photocatalytic properties and photoinduced hydrophilicity of surface-fluorinated TiO2, Chem. Mater. 19 (2007) 116–122, https://doi.org/10.1021/cm061855z.
[62] T.D. Kusworo, Qudratun, D.P. Utomo, Performance evaluation of double stage process using nano hybrid PES/SiO2-PES membrane and PES/ZnO-PES membranes for oily waste water treatment to clean water, J. Environ. Chem. Eng. 5 (2017) 6077–6086, https://doi.org/10.1016/j.jece.2017.11.044.
[63] Z. Zabihi, M. Homayoonfal, F. Davar, Application of UV irradiation enhanced by CuS photosensitive nanoparticles to mitigate polysulfone membrane fouling, J. Photochem. Photobiol. Chem. 390 (2020), 112304, https://doi.org/10.1016/J.JPHOTOCHEM.2019.112304.
[64] P. Veisi, M.S. Seyed Dorraji, M.H. Rasoulifard, S. Ghaffari, A. Khobkar Choobar, Synergistic photocatalytic-adsorption removal effect of NiFe2O4-Zn-Al mixed metal oxide composite under visible-light irradiation, J. Photochem. Photobiol. Chem. 414 (2021), 113268, https://doi.org/10.1016/j.jphotochem.2021.113268.
[65] F. Dalanta, T.D. Kusworo, Synergistic adsorption and photocatalytic properties of AC/TiO2/CeO2 composite for phenol and ammonia–nitrogen compound degradations from petroleum refinery wastewater, Chem. Eng. J. 434 (2022), 134687, https://doi.org/10.1016/J.CEJ.2022.134687.
[66] R. Molinari, M. Mungari, E. Drioli, A. di Paola, V. Loddo, L. Palmisano, M. Schiavello, Study on a photocatalytic membrane reactor for water purification, Catal. Today 55 (2000) 71–78, https://doi.org/10.1016/S0920-5861(99)00227-8.
[67] H. Zhang, X. Quan, S. Chen, H. Zhao, Y. Zhao, Fabrication of photocatalytic membrane and evaluation its efficiency in removal of organic pollutants from water, Separ. Purif. Technol. 50 (2006) 147–155, https://doi.org/10.1016/J.SEPPUR.2005.11.018.
[68] H. Zhang, X. Quan, S. Chen, H. Zhao, Y. Zhao, The removal of sodium dodecylbenzene sulfonate surfactant from water using silica/titania nanorods/nanotubes composite membrane with photocatalytic capability, Appl. Surf. Sci. 252 (2006) 8598–8604, https://doi.org/10.1016/J.APSUSC.2005.11.090.
[69] Y. Gao, M. Hu, B. Mi, Membrane surface modification with TiO2–graphene oxide for enhanced photocatalytic performance, J. Membr. Sci. 455 (2014) 349–356, https://doi.org/10.1016/J.MEMSCI.2014.01.011.
[70] H. Song, J. Shao, J. Wang, X. Zhong, The removal of natural organic matter with LiCl–TiO2-doped PVDF membranes by integration of ultrafiltration with photocatalysis, Desalination 344 (2014) 412–421, https://doi.org/10.1016/J.DESAL.2014.04.012.